2-Azabutadiene complexes of rhenium(I): S , N -chelated species with photophysical properties heavily governed by the ligand hidden traits

Adrien Schlachter, Frank Juvenal, Rodolphe Kinghat Tangou, Abderrahim Khatyr, Fabrice Guyon, Paul-Ludovic Karsenti, Carsten Strohmann, Marek Kubicki, Yoann Rousselin, Pierre Harvey, et al.

2-Azabutadiene complexes of rhenium(i): S,N-chelated species with photophysical properties heavily governed by the ligand hidden traits

Adrien Schlachter,[a] Frank Juvenal,[a] Rodolphe Kinghat Tangou,[b] Abderrahim Khatyr,*[b] Fabrice Guyon,[b] Paul-Ludovic Karsenti,[a] Carsten Strohmann,[c] Marek M. Kubicki,*[d] Yoann Rousselin,[d] Pierre D. Harvey*[a] and Michael Knorr*[b]

[a]*Département de Chimie, Université de Sherbrooke, Sherbrooke, Québec, Canada J1 K 2R1*

[b]*Institut UTINAM, UMR CNRS 6213, Université Bourgogne Franche-Comté, 25030 Besançon, France* ***E-mail:*** *michael.knorr@univ-fcomte.fr*

[c]*Anorganische Chemie, Technische Universität Dortmund, 44227 Dortmund, Germany*

[d]*Institut de Chimie Moléculaire UMR 5260, Université Bourgogne Franche-Comté, 21078 Dijon, France*

Abstract

The reaction of $[Re(CO)_3(THF)(\mu\text{-}Br)]_2$ or $[Re(CO)_5X]$ (X = Cl, Br, I) with the diaryl-2-azabutadienes $[(RS)_2C{=}C(H){-}N{=}CAr_2]$ containing two thioether arms at the 4,4-position forms the luminescent *S*,*N*-chelate complexes *fac*-$[(OC)_3ReX\{(RS)_2C{=}C(H){-}N{=}CAr_2\}]$ (**1a–h**). The halide abstraction by silver triflate converts $[(OC)_3ReCl\{(PhS)_2C{=}C(H){-}N{=}CPh_2\}]$ (**1c**) to $[(OC)_3Re(OS(=O)_2CF_3)\{(PhS)_2C{=}C(H){-}N{=}CPh_2\}]$ (**1j**) bearing a covalently bound triflate ligand. The cyclic voltammograms reveal reversible S^N ligand-centred reduction and irreversible oxidation waves for all complexes. The crystal structures of nine octahedral complexes have been determined along with that of $(NaphtylS)_2C{=}C(H){-}N{=}CPh_2$ (**L6**). A rich system of weak non-covalent intermolecular secondary interactions through CH···X(Cl, Br)Re, CH···O, CO···π(Ph), CH···πCO, CH···O and CH···S contacts has been evidenced. The photophysical properties have been investigated by steady-state and time-resolved absorption (fs transient absorption, fs-TAS) and emission (ns-TCSPC and ps-Streak camera) spectroscopy in 2-MeTHF solution at 298 and 77 K. The emission bands are composed of either singlet ($450 < \lambda_{max} < 535$ nm) and/or triplet emissions (at 77 K only, $\lambda_{max} < 640$ nm, or appearing as a tail at $\lambda > 600$ nm), which decay in a multiexponential manner for the fluorescence (short ps (*i.e.* <IRF) $< \tau_F < 1.9$ ns at 298 and 77 K) and monoexponentially for the phosphorescence ($4.0 < \tau_P < 7.0$ ns at 77 K). The fs-TAS data reveal the presence of 2 to 4 transient species decaying in four narrow time windows (generally 125–165 fs, 370–685 fs, 3–6 ps, 30–45 ps). The

complexity of these kinetics was explained by studying the photophysical behaviour of ligand **L6**. Its behaviour is the same as the complexes thus indicating that the ligand dictates the kinetic traits of the Re-species, except for the triplet emission as **L6** is not phosphorescent. The triplet lifetime ($4.0 < \tau_P < 7.0$ ns) is considered very short but not unprecedented. Furthermore, the nature of the lowest energy excited states of these chelate compounds and **L6** has been addressed using DFT and TDDFT calculations and been assigned to metal-to-ligand (MLCT) and/or intraligand charge-transfer (ILCT).

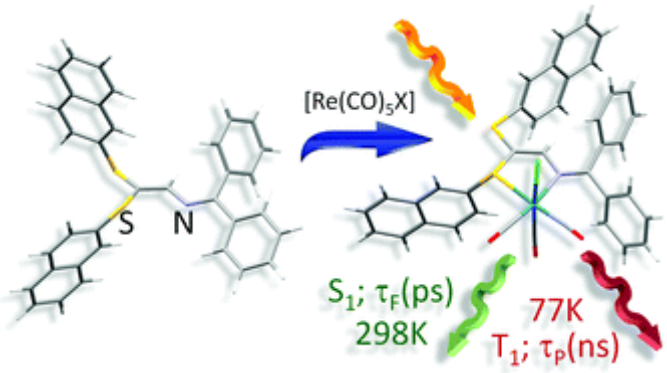

Introduction

The *fac*-halotricarbonyl(diimine)rhenium complexes (X = Cl, Br, I) and their related derivatives exhibit remarkable photophysical properties[1–3] and numerous applications in photocatalysis, namely for CO_2 reduction,[4–9] singlet oxygen generation photodynamic therapy,[10–14] dye sensitized solar cells (DSSCs) and organic photovoltaic devices,[15–20] emitters in OLED devices,[21,22] CO photodelivery,[23] labels for biomolecules[24] and medicinal imaging,[25–31] have recently been reported. Moreover, two-photon absorption,[32,33] nonlinear optical,[33–36] and upconversion[37,38] properties are also known, and the intramolecular photophysical properties are often governed by ultrafast excited state kinetics (fs and ps).[39–42]

In quest of finding new chelating ligands for the preparation of emissive transition metal-containing chromophores, some of us explored the coordination chemistry of these ditopic diaryl-2-azabutadiene-4,4-dithioether featuring soft S-donor sites and a harder imine-type N-donor site with copper(i), molybdenum(0), palladium(ii) and platinum(ii).[43–45] However, the photochemical properties of these N^S chelate complexes or cyclometallated species has not been systematically explored. In contrast with the phletora of N^N-chelated Re(i) species, (N^S)-chelated Re(i) complexes are quite rare.[46–50] It is noteworthy that despite the striking structural similitude with the generally strongly emissive *fac*-halo(diimine)tricarbonylrhenium(i) complexes, these scarce reports on the Re(N^S)-containing

species do not mention any particular evidence for luminescence. Concurrently, in search of new emissive metal/(N^S)-containing materials, the *fac*-bromotricarbonyl(N^S)rhenium(i) complex issued from the complexation of diphenyl-2-azabutadiene-4-chloro-4-phenylthioether, was reported,[51] and exhibits a structured emission band at 616 nm. No further photophysical study was undertaken.

This preliminary result prompts for a throughout investigation of this novel family of complexes and we now report a series of *fac*-halotricarbonyl(N^S)rhenium(i) complexes where the chelating ligands (N^S) are various diaryl-2-azabutadiene-4,4-dithioethers leaving a dangling thioether arm. To fine-tune the steric and electronic properties of the ligands, an extended series of functionalized aza-butadienes with SR groups bearing alkyl and aryl groups has been synthesized. Moreover, the impact of the Re–X ligand has been systematically varied (X = Cl, Br, I, OTf; Schemes 1–3). These new complexes were fully characterized, including X-ray structure diffraction and electrochemistry, and exhibit singlet and triplet intraligand and/or metal-to-ligand charge-transfer emissions. Their excited state properties turn out to be entirely dominated by the structural features of the flexible ligands and the concurrent photophysical events are found ultrafast. Notably, their phosphorescence lifetimes at 77 K are notoriously short-lived (~5.5 ± 1.5 ns), but not unprecedented, in comparison with the µs timescale generally encountered for the *fac*-halotricarbonyl(diimine)rhenium homologues at this same temperature.[52–59]

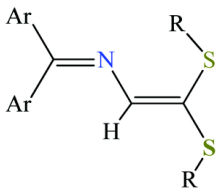

L1 : Ar = Ph, R = *i*Pr
L2 : Ar = Ph, R = Ph
L3 : Ar = Ph, R = *p*-Tol
L4 : Ar = Ph, R = *n*Bu
L5 : Ar = Cl-C_6H_4, R = *p*-Tol
L6 : Ar = Ph, R = Naphtyl

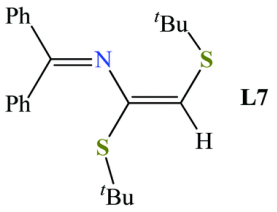

L7

Scheme 1 Structural formulas for the free ligands used in this work.

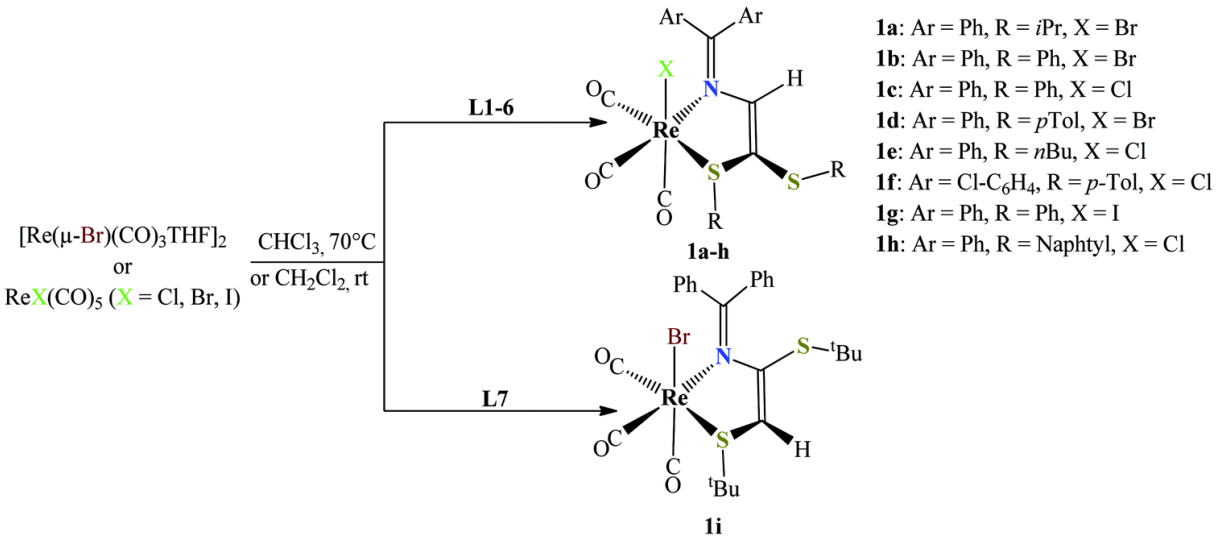

Scheme 2 Reaction schemes for the synthesis of complexes **1a–i**.

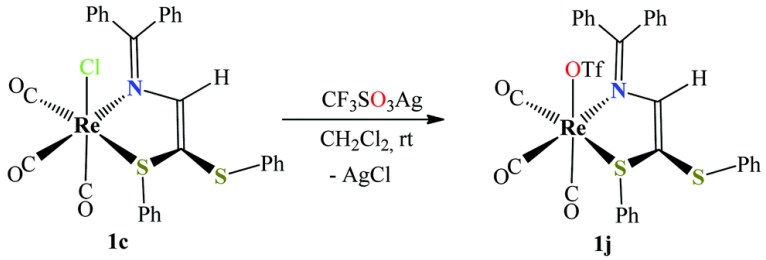

Scheme 3 Reaction schemes for the synthesis of complex **1j**.

Results and discussion

Synthesis of compound and structural characterization

The ligands were prepared and purified according to the procedure previously published by our group (Scheme 1).[43,50] This panel of ligands **L1–L5** bearing both aliphatic and aromatic thioether functions allows for the modulation of the donor propensity of the SR groups. This series was extended to (NaphtylS)$_2$C=C(H)–N=CPh$_2$ (**L6**) bearing two SNaphtyl groups, which may act as potential chromophores (see Photophysical section).

L6 was straightforwardly obtained by reacting Cl$_2$C=C(H)–N=CPh$_2$ with an excess of *in situ* prepared thiolate NaSNaphtyl in DMF. The molecular structure of **L6** was deduced by X-ray crystallography, and selected metric parameters are provided in Fig. 1. Its geometry is reminiscent to that of other structurally characterized (ArS)$_2$C=C(H)–N=CPh$_2$ ligands[60] and the imine unit bears one phenyl ring (C8 as C$_{ipso}$ atom), which is roughly coplanar (25.3(2)°) with the azabutadiene array while the second ring (C1 as C$_{ipso}$) forms an angle of 65.5(1)° with this plane. The C7–N–C14–C15 torsion angle of 175(7)° indicates an extended π-electron

delocalization over the central skeleton. The small dihedral angle between naphthyl average planes (9.86(6)°) and a C16···C26 distance of 3.167(5) Å, significantly shorter than the sum of van der Waals radii suggest, at first glance, the presence of intramolecular π–π interaction or π-stacking. However, the conformation of the naphthyl groups, estimated from the rather large C16–S1···S2–C26 torsion angle of 62.6(2)°, causes a slippage that does not favor an effective π–π overlap. Considering only the phenyl parts of the naphthyl groups (Fig. S1a and S1b‡), the inter-plane dihedral angle is 9.84(6)°, the centroid-to-centroid distance is 3.997(2) Å and the shift parameters are equal to 2.438(5) and 2.275(5) Å. These geometrical features may indicate the presence of a weak π–π slipped interaction. However, an Atoms In Molecules analysis[61] of the wavefunction calculated (diffuse and polarized large 6-311G++(d,p) basis set) for the X-Ray molecular geometry shows no bond critical point (Fig. S1c‡) between the two naphthyl planes and thus does not confirm an effective electronic interaction (other AIM studies related to this manuscript will be presented elsewhere). Noteworthy, an intermolecular π–π interaction between *ortho*-C13 carbon atom of one phenyl group with the C14=C15 bond of a neighbor molecule is observed (Fig. S2c‡). Various C–H···π contacts complete the building of the rich 3D structure (an example of dimer fragment is shown in Fig. S2a and S2b‡).

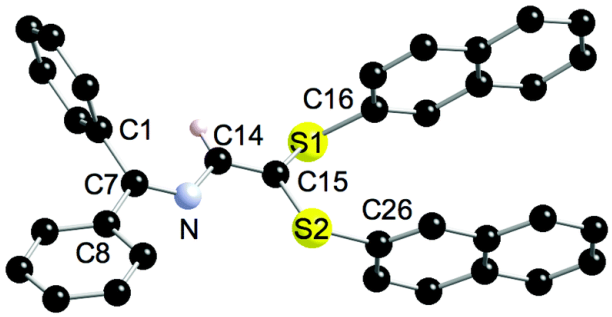

Fig. 1 Molecular structure of **L6**. Apart of the vinylic H atom, all other H atoms are omitted. Selected bond lengths [Å] and angles [°]: C7–N 1.291(3), N–C14 1.390(3), C14–C15 1.347(4), C15–S1 1.757(3), C15–S2 1.768(3); C1–C7–C8 116.6(2), C1–C7–N 126.2(2), C8–C7–N 117.1(2), C7–N–C14 122.0(2), C14–C15–S1 118.7(2), C14–C15–S2 117.8(2), S1–C15–S2 123.38(17).

The target tricarbonyl Re-complexes **1a–h** were prepared by reacting the ligands **L1–7** with the dimer $[Re(\mu\text{-}Br)(CO)_3(THF)]_2$[62] in dichloromethane at room temperature or with the mononuclear precursor $ReX(CO)_5$ (X = Cl, Br or I) in chloroform at 70 °C (Scheme 2). All complexes were isolated as air stable red crystalline solids (**1a–g**), except for and **1h** which was

yellow, with 70–80% yields upon breaking the μ_2-Br bridge or by thermal substitution of two carbonyls of the $ReX(CO)_5$ complexes.

Complex **1j** (Scheme 3) was synthesized by reacting the complex [$ReCl(CO)_3\{(Ph_2C{=}N{-}CH{=}C(SPh)_2\}$] (**1c**) with silver triflate in dichloromethane at room temperature and was isolated in the form of orange coloured crystals. The coordination of one of the triflate oxygens on Re was also confirmed by an X-ray diffraction study (see below).

All compounds are highly soluble in halogenated solvents and photostable over prolonged periods of time. They were characterized by ^1H and $^{13}C\{^1H\}$ NMR, UV-vis and IR spectroscopy and the data are consistent with the proposed structures (see Table S1‡ for selected spectroscopic data). The positions of the three CO stretching vibration peaks of all complexes are similar to those observed for the *fac*-[$ReBr(CO)_3\{(PhSCH_2)_2SiPh_2\}$][63] and [$ReX(CO)_3$(dithioether)][$MX(CO)_3$(diselenoether)] (M = Mn, Re, X = Cl, Br and I).[64–66] Noteworthy, neither the variation of the terminal substituent on sulfur or the nature of the halide significantly influences the C=O stretching frequencies. The only exception is observed for complex **1j** (X = OTf) which, in comparison with the other complexes, exhibits a slight hypsochromic shift of approximately 10 cm^{-1} for the three ν(CO) stretching bands. The ^{13}C chemical shifts of the complexes **1a–j** match well those reported for other *fac*-rhenium(i) carbonyl complexes.[67] The observation of three distinct carbonyl resonances indicates that no C=O scrambling occurs at ambient temperature. Substitution of chloride in complex **1c** by the triflate anion was confirmed by the observation of a quartet in the NMR $^{13}C\{^1H\}$ spectrum of complex **1j**, displaying a coupling constant $^1J_{C-F}$ = 319 Hz.

Crystal structure determinations

The crystal structures of nine derivatives of **1** were determined and analyzed. They exhibit a slightly distorted *fac*-octahedral geometry, in which three *facial* carbonyl groups, one bidentate *S*,*N*-azabutadiene chelate and one halide (triflate in e of **1j**) complete the coordination sphere around the central Re(i) atom. A typical example of a solid-state structure is that of the bromo derivative **1a** shown in Fig. 2 (left). The exceptional e of complex **1i** chelated by the **L7** ligand, bearing, for steric reasons, the ^{t}Bu groups at two adjacent C atoms of the azadienic chain, is shown in Fig. 2 (right).

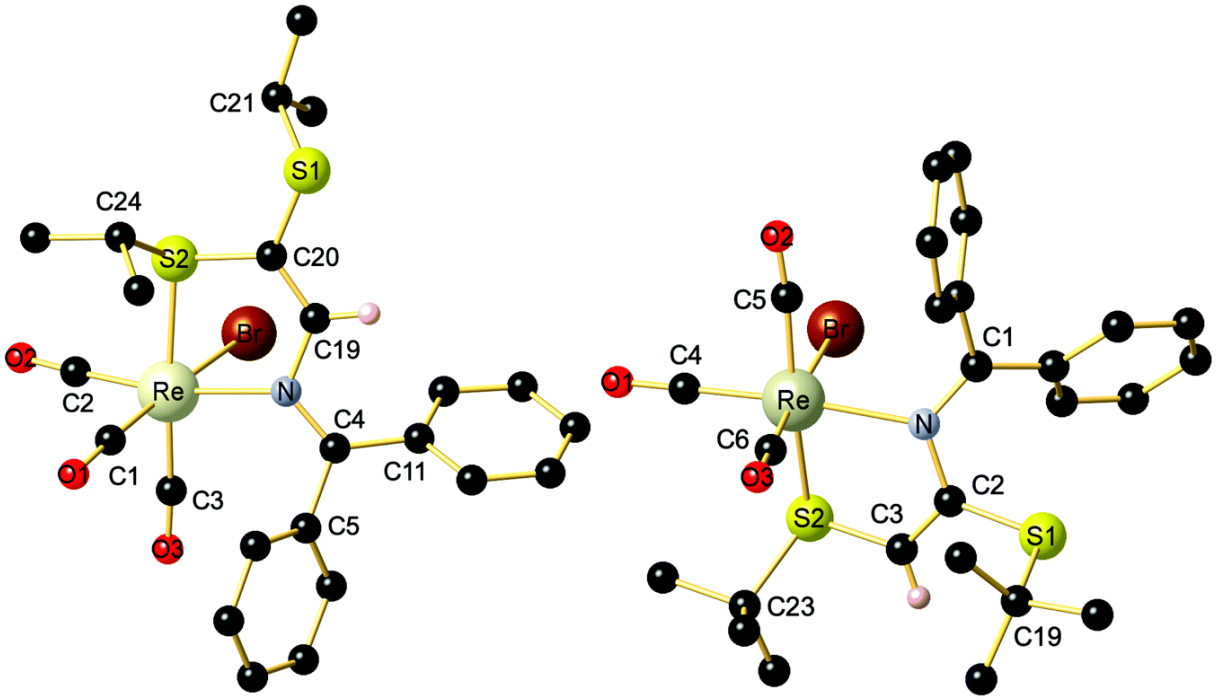

Fig. 2 Comparison of the molecular structures of **1a** (bearing two geminal SR groups (left) and **1i** bearing two vicinal SR groups (right). Selected bond lengths [Å] and angles [°] for **1a**: Re–Br 2.6293(4), Re–C1 1.908(3), Re–C2 1.907(3), Re–C3 1.924(3), Re–N 2.249(3), Re–S2 2.4585(7), C4–N 1.310(3), N–C19 1.415(3), C19–C20 1.336(3), C20–S1 1.758(2), C20–S2 1.775(2), S1–C21 1.842(3), S2–C30 1.842(3); N–Re–S1 79.63(5), Br–Re–S1 82.14(2), Br–Re–N 80.26(5), Re–N–C4 124.34(16), Re–N–C5 115.49(14), Re–S1–C6 100.09(8), Re–S1–C7 116.44(9), S1–C6–S2 119.15(13). Selected bond lengths [Å] and angles [°] for **1i**: Re–Br 2.6210(4), Re–C4 1.898(4), Re–C5 1.944(4), Re–C6 1.918(5), Re–N 2.258(3), Re–S2 2.4756(10), C1–N 1.324(5), N-C2 1.430(5), C2–C3 1.341(6), C2–S1 1.779(4), S2–C3 1.751(4); N–Re–S2 78.29(8), Br–Re–S2 81.70(2), Br–Re–N 83.57(8), Re–N–C1 121.8(3), Re–N–C2 116.4(2), Re–S2–C3 98.96(15), N–C2–S1 119.5(3), N–C2–C31 120.3(3).

The plots for all other complexes (except **1e**, *vide infra*) are gathered in Fig. S3–S8 in the ESI.‡ Despite the noticeable differences of steric requirements, flexibility and donor propensities of the R groups bound to the S atoms, the bond lengths and angles within the coordination sphere of the metallic atom are not influenced by the nature of the R groups and vary very little from one complex to another. In fact, the Re–S bond lengths (2.454(1)–2.476(1) Å), Re–N (2.223(3)–2.260(10) Å), Re–Br (2.6210(4)–2.6295(6) Å) and Re–Cl (2.4803(15)–2.495(2) Å) fall into the narrow ranges. Selected bond lengths and angles are provided in Table S2.‡ Even for complex **1i** bearing a bulky and rigid ^{t}Bu-S substituent at two adjacent ethylenic C atoms of the azabutadiene array, the bond lengths do not deviate significantly from typical

values. These observations also apply for the bond angles with an emphasis on the X–Re–C (*trans*-CO 173.5(1)–177.5(2)°) and on the S–Re–N bite angles, which vary from 78.29(8) (**1i**) to 80.78(17)° (**1g**). With the exception of the particular e of **1i** (R = ^{t}Bu), there seems to be a good delocalization of electron density (π conjugation) over the central skeleton of the azabutadiene ligand as deduced from the C=N–C=C torsion angles ranging from 168.9(3)° (**1e-tricl**) to 180.0(8)° (**1g**) (Table S3‡). However, the near coplanarity of the phenyl ring placed on the side of the imine nitrogen lone pair with the C=N–C=C plane depicted in free AzBu molecules, no longer exists in the complexes. The corresponding dihedral angles are close to 60° (Table S3‡) instead of 15°–25°, often observed for the free ligands (see *e.g.* compound **L6**). This may be the consequence of the involvement of the imine-type nitrogen lone pair to the bonding with the bulky $ReX(CO)_3$ unit. The relative conformation of SR groups in these dithioether-functionalized 2-aza-1,3-butadienes deduced by the C–S···S–C torsion angles (C is the C_{ipso} carbon atom of R group; Table S3‡), is another interesting geometric parameter and will be addressed in detail in the Photophysical and computational studies section of the ligand **L6**.

The conformation of the $[(SNapht)_2]$ unit of complex **1h** noted by the C–S···S–C torsion angle within the crystal differs significantly from that in the free ligand [133.1(2) *vs.* 62.6(2)°]. In the four complexes chelated by ligand **L2**, the torsion angles of the $[(SPh)_2]$ unit vary from 71.6° to 118.5° (65.7(2)° in the free ligand[50]). Conversely, the conformation of **L1** as a free ligand and in its complex **1a** are very similar (107.0(2) and 104.5(1)°, respectively). These observations suggest that the conformation of the SR groups is not an intrinsic molecular property but is rather influenced by weak non-covalent packing forces in the crystals. Since the chelating AzBu ligands contain two different coordinating sites (*S* and *N*), the molecular symmetry is C_1 and the complexes bear an intrinsic chirality. Because all complexes crystallize in space groups containing improper symmetry operations (symmetry centers and/or planes), both *S* and *R* enantiomers are always present. Consequently, all crystals are racemic.

It is worth noting that two different polymorphs have been identified for complex **1e** by X-ray diffraction carried out on two different samples obtained from CH_2Cl_2/heptane and $CHCl_3$/heptane mixtures (Fig. 3). These phases crystallize in the monoclinic $P2_1/n$ and the triclinic $P2_1/n$ space groups and differ by 68 $Å^3$ (2.5%) in unit cell volumes. Both *S* and *R* isomers are present in the asymmetric unit of the triclinic structure. The metric parameters in both structures are similar but the intermolecular interactions building the supramolecular architecture are completely different and are certainly responsible of the

difference of unit cell volumes. There are also two independent complex molecules in the asymmetric unit of the structure of **1g**.

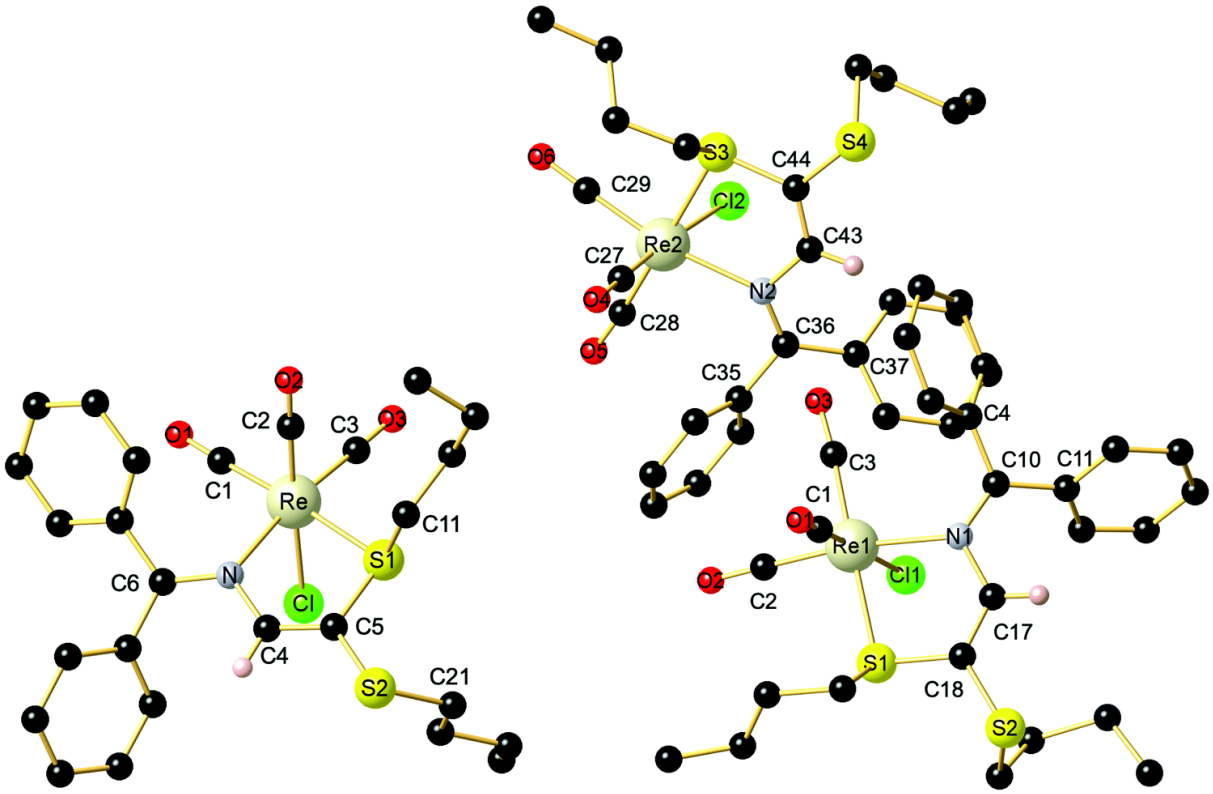

Fig. 3 Molecular structure of the monoclinic polymorph of **1e-mono** (left, enantiomer *S* from the asymmetric unit is shown), two independent molecules (enantiomers *R* and *S*) present in the asymmetric unit of **1e** in the triclinic phase **1e-tricl** (right). Selected bond lengths [Å] and angles [°] for **1e-mono**: Re–Cl 2.4875(11), Re–C1 1.936(5), Re–C2 1.903(5), Re–C3 1.921(5), Re–N 2.259(4), Re–S1 2.4557(11), C6–N 1.332(6), N–C4 1.406(5), C5–C4 1.326(6), C5–S1 1.770(4), C5–S2 1.756(4); N–Re–S1 79.81(9), Cl–Re–S1 82.57(4), Cl–Re–N, 80.69(9), Re–N–C6 125.8(3), Re–N–C4 114.2(3), Re–S1–C5 99.05(15), Re–S1–C11 112.28(15), S1–C5–S2 118.2(2).

As mentioned, the bond lengths and angles are relatively constant in all complexes. However, the crystal packing and the nature of non-covalent intermolecular interactions differ significantly. The types of interactions observed in complexes **1a–1j** are provided in Table S4‡ and shown in Fig. S9–S18.‡ CH···π(aromatic rings) and CH···X–Re interactions are frequently observed, except for the iodo complex **1g** and the bromo complex **1i** (with bulky R = ^{t}Bu substituent) for which CH···X–Re contacts are not observed. A halogen bonding involving the X atom bound to Re is not observed. However, its presence may be tentatively suggested for the C-bonded chlorides in **1f** and **1j** (Fig. S14 and S18‡). If in **1f**, the angle C–Cl

(PhCl substituent)···O(CO) of 154.4° deviates considerably from the ideal value of 180°, in **1j**, where the C–Cl (CH_2Cl_2 solvent)···F(triflate) angle amounts to 168.2°, the deviation is smaller. It is worth noting that in spite of the presence of several aromatic groups, a π-stacking through overlap of these rings is almost absent. The sole example can be found in the structure of complex **1g**, in which the SPh substituents bound to the Re1 and Re2 atoms form dimers (over the centers of symmetry), which may be considered as slipped π–π overlaps with the centroid to centroid distances of 4.131 (Re1) and 4.049 Å (Re2) and the shift parameters equal to 1.712 and 1.632 Å, respectively (Fig. S16d and S16e‡).

Photophysical and computational studies

Absorption and emission spectra of the imine-thioether ligand L6

The basic motif of the imine-thioether consists of an azadienic Ph_2C=N–CH=C(SNapht)$_2$ backbone. Despite its striking structural simplicity, this organic chromophore has never been investigated in a photophysical standpoint. One related organic compound, Ph_2C=N–CH=C(SPh)Cl, has been reported to be emissive at 298 K in CH_2Cl_2 (λ_{max} = 450 nm) but no assignment was proposed.[51,68] This ligand, **L6**, is weakly emissive in solution at 298 K, but is found fluorescent in the solid state and in frozen solution at 77 K (Fig. 4a–c). This assignment is based on the expected position of the 0–0 component of the absorption and fluorescence bands (~430 nm), its calculated position of the pure electronic transition (0–0 ~400 nm, TDDFT, below), and the emission decay constant (below). The fluorescence band of solid **L6** appears broad. The fluorescence decay of **L6** in 2-MeTHF at 298 K is ultrafast (<10 ps), which is consistent with the low intensity of this emission (note that the small mismatch of the steady state and time-resolved spectra is due the fact that the steady state and time-resolved spectra are respectively corrected and uncorrected for instrument responses). The decay associated spectra, DAS, at 77 K indicate the presence of three emitting species with decay time constants of <10, 96 and 697 ps (Fig. 4d, Table 1). The former signal (<10 ps) spans from 450 to 620 nm and is very weak, which causes a heavily distorted band to the temporal dispersion of the instrument. Using TCSPC (laser pulse width ~90 ps), three components were depicted (110 ps, 440 ps and 1.68 ns) and the decay trace is placed in Fig. S19.‡ The latter one was not observed by the Streak camera probably due to its intrinsic weak intensity (B_i value = 0.001). Using fs-TAS, four transient species decaying with time constants of 201 fs, 664 fs, 6.4 ps and 75 ps were also observed (Fig. 4e and f). Again, the latter one appears to be similar (*i.e.* the same species presumably) to that observed by Streak camera (96 ps) and TCSPC (110 ps). The

timescales of sub- and short-ns is consistent with a S_1 emission but are clearly on the short side. The fluorescence decay time constants of **L6** in the solid-state are expectedly longer than those in solution due to increase in medium rigidity. These decays are also found multi-exponentials, and the resemblance of the time constants of **L6** in solution and in the solid state is striking, also suggesting the presence of multiple conformations. This hypothesis was checked by comparing the experimental X-ray powder diffraction pattern with that of the calculated one from the single crystal data at the same temperature (Fig. S21‡). The experimental trace exhibits an amorphous domain recognizable from the ill-defined baseline. Moreover, several supplementary diffraction peaks, absent from the calculated trace, appear in the pattern. Together, these features indicate the presence of more than one species, here associated with conformers.

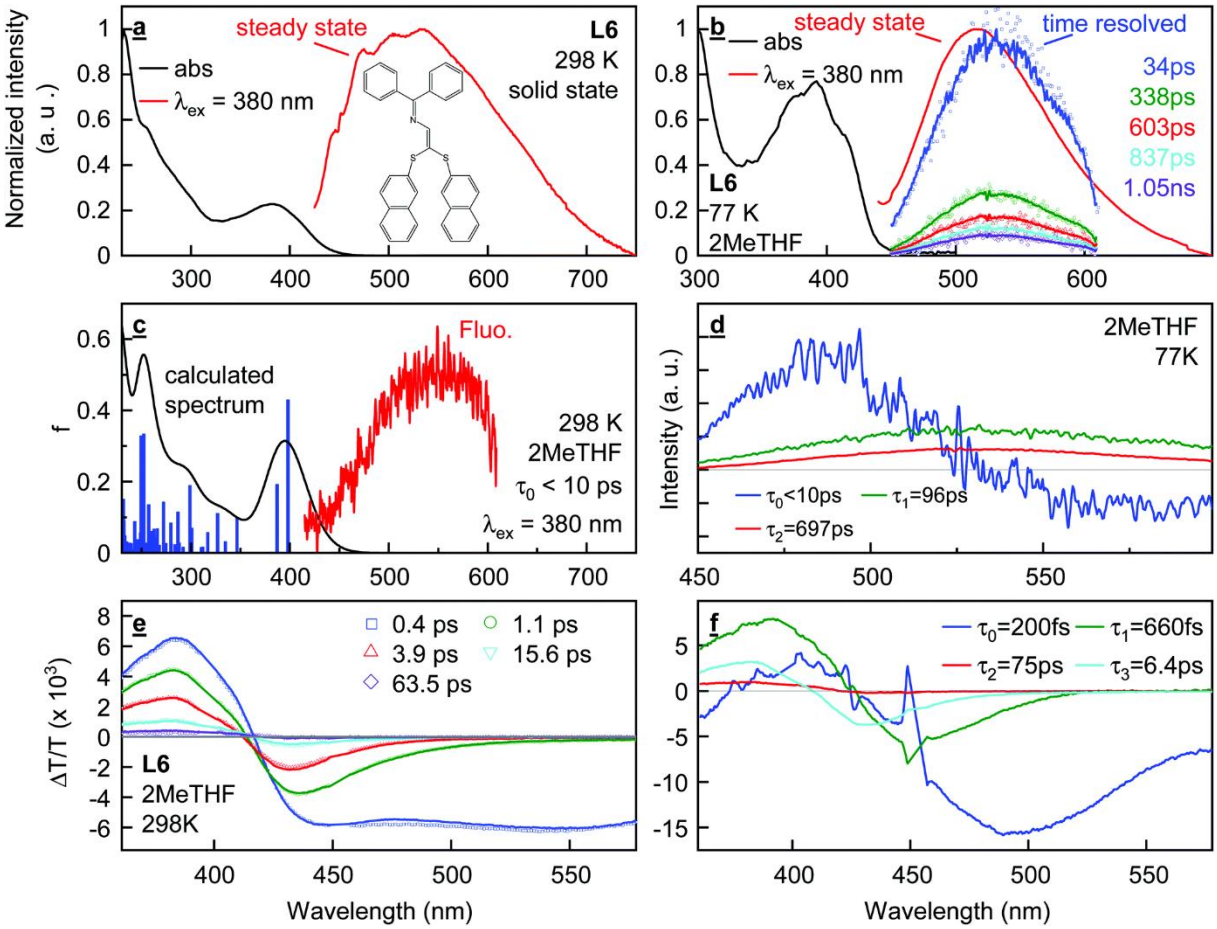

Fig. 4 a: Solid state absorption (black) and fluorescence (red) spectra of **L6**. b: Absorption (black), steady state fluorescence (red), and time-resolved emission spectra (various colours) of **L6** in 2-MeTHF at 77 K. Note: The Streak camera spectra are uncorrected for the instrument response. c: Left: Calculated absorption spectrum of **L6** by TDDFT; the bar graph (blue) reports the oscillator strength (f) and positions of the 100st electronic transitions. An arbitrary thickness

of 3000 cm^{-1} is assigned to each bar for the spectrum simulation. Right fluorescence spectrum of **L6** (2-MeTHF; 298 K; Streak camera; λ_{exc} = 397 nm, note that the spectra are not corrected for the PMT response). d: Decay associated spectra of **L6** in 2-MeTHF at 77 K (λ_{exc} = 397 nm). e: Evolution of the fs-TAS of **L6** in 2-MeTHF(λ_{exc} = 397 nm). f: DAS of the fs-TAS of **L6** in 2-MeTHF. Note that the positive and negative responses represent the bleached and transient signals, respectively.

Table 1 Fluorescence (τ_F) and excited state (τ_e) lifetimes of **L6** in 2-MeTHF and in the solid state[a,b]

Temp.	**Conditions**	**τ_F in ps (Streak)**			**τ_F in ns (TCSPC)**		
298 K	2-MeTHF	<10			<0.12 (*i.e.* IRF)		
298 K	Solid state	9.8[c]		286[d]	<0.12 (*i.e.* IRF)		
Temp.	**Conditions**	**τ_F in ps (Streak)**			**τ_F in ns (B_i, f (%)), χ^2 = 1.044 (TCSPC)**		
77 K	2-MeTHF	<10	96[d]	697[d]	0.11 (0.019, 31)	0.44 (0.006, 36)	1.68 (0.001, 33)
77 K	Solid state	<10	132[d]	736[d]	<0.12 (*i.e.* IRF)		
Temp.	**Conditions**				**τ_e fs-TAS**		
298 K	2-MeTHF				200 fs, 660 fs, 6.4 ps, 75 ps		

a $f_i(\%) = (B_i\tau_i)/\sum(B_i\tau_i)\cdot 100\%$; $I_e(t) = B_1\exp(-t/\tau_1) + B_2\exp(-t/\tau_2) + B_3\exp(-t/\tau_3)$+. b The correspondence between the Streak camera and TCSPC data are respectively as follow: 96 ps *vs.* 110 ps, and 700 ps *vs.* 440 ps. The discrepancy is explained by the large uncertainties related to deconvolution of multi-exponential decays. c The IRF is 6.6 ps in this e. d Weak component.

Based on these steady-state and time-resolved absorption and emission properties, two questions arise: are these multiple lifetimes associated with multiple singlet excited states or different conformers and what the nature(s) of the emissive excited state(s) is (are)? These questions are addressed by DFT and TDDFT computations. Firstly, the origin of the multiple exponential fluorescence decays is addressed. Fully optimized geometries of various conformations were computed (DFT; Fig. 5). **L6** as well as all ligands used to build the complexes exhibit multiple single bonds (*i.e.* rotors; 2 Ph–C, 2 C–S, 2 S–aryl for **L6**). Four conformations were computed (see their total energies in a.u.) and the most stable one is conformer 1 (E_{TOT} conformer 1 < conformer 2 < conformer 4 < conformer 3; by 0.0017, 0.0202 and 0.8434 kJ mol^{-1}, respectively. This list of conformers is obviously not exhaustive, but this sampling is large enough to provide a secure conclusion. Moreover, it also confirms the

conclusion made from the X-Ray structures (*vide supra*) that there is no π interactions between the naphthyl planes and that the actual conformation depends on weak crystal packing forces.

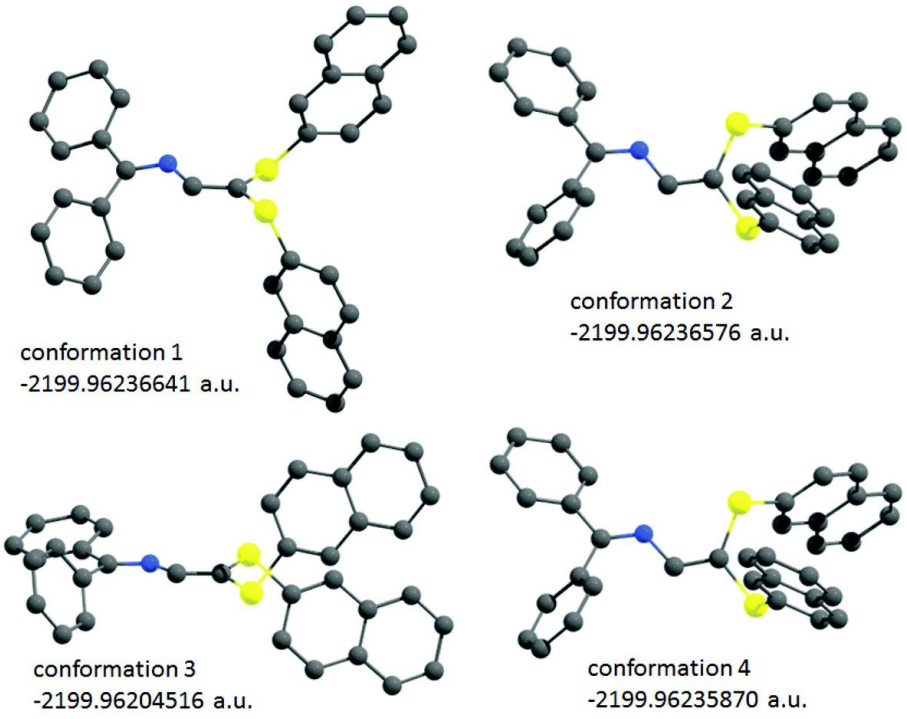

Fig. 5 Optimized geometry and their total DFT energy of four possible conformers of **L6**.

The close proximity in total energy and the relatively low barrier to rotation around the C–S and C–aryl single bonds, suggest that these species co-exist in solution. The fact that the excited state lifetimes are all ≤75 ps at 298 K (fs-TAS data, Table 1) indicates that molecular torsions contribute efficiently to the non-radiative rate constant, k_{nr}. This observation is also corroborated by the large increase in τ_F when **L6** is placed in rigid glasses at 77 K; τ_F = 0.7 ns (Streak) or ~1.7 ns (TCSPC).

For the second question on the nature of the lowest-energy singlet state, DFT computations using the X-ray structural data indicate that the atomic contributions spreading over the two phenyls, central C=N–(H)C=C core, and thionaphthyls are respectively 9, 23 and 68% (HOMO) and 33, 44 and 23% (LUMO; Fig. 6). So, the HOMO → LUMO transition creates a charge transfer excited state [C=N–(H)C=C] to coplanar phenyl group mostly. Moreover, the calculated position of the spin-allowed lowest energy transition is ~417 nm (oscillator strength, f = 0.7222) based on TDDFT computations. The latter corresponds to a HOMO → LUMO transition (with a contribution of 97%; detail in the ESI, Fig. S22–S25, Tables S8 and S9‡). This S_1 state is well isolated from any other excited states as the next transition is predicted to be at 374 nm. This means that upon exciting at 397 nm (see caption of Fig. 4), only

the S_1 state is selectively populated. Upon assigning an arbitrary thickness of 3000 cm^{-1} to each calculated transition (*i.e.* each bar), a simulated spectrum is generated (Fig. 4c), which matches reasonably well with the experimental data.

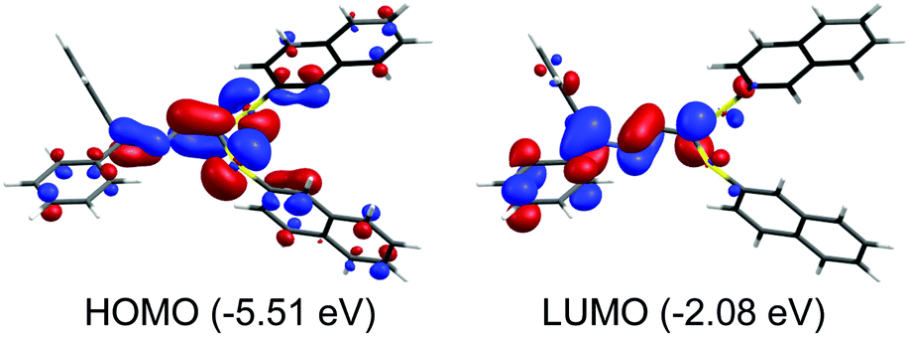

Fig. 6 Representations of the HOMO and LUMO of **L6** (a THF solvent field was applied). See ESI‡ for other frontier MOs. The X-ray structure was used for the geometry optimization as the geometry in solution is unknown and is most likely multiple.

Absorption and emission spectra of the rhenium imine–thioether complexes

Prior to discussing the photophysical properties of the target complexes, a reminder of the corresponding properties of homologous diimine *fac*-halotricarbonyl(bipyridine)rhenium(i) is appropriate. Using fs-fluorescence up-conversion technique, the band maxima of the fluorescence has been detected in the vicinity of 540–550 nm and found to decay in the fs time scale.[69] More accurately, this fluorescence decays are biphasic with time constants τ_1 = 85–150 fs, and τ_2 = 340–1200 fs.[70] This ultrafast relaxation process stems from an efficient intersystem crossing using strong spin-vibronic couplings,[71,72] which occur as fast as 100 fs (X = Cl).[73] Concurrently, for some other derivatives belonging to this same family, using ps time-resolved IR spectroscopy, their triplet excited states have been found to be very short lived (*i.e.* from 1 ps to 1800 ps) at 298 K.[2,69,73–75] The proximity of the fs luminescence (540–550 nm) and ps emission (~550–600 nm) bands[71,72] may ocionally lead to confusion between the two. For example, a recent report on $ReCl(CO)_3$(2-Py-HC=N-2-C_6H_4-SR) complexes (R = Me, Et), indicated that the emission quantum yields are 0.013–0.014 and lifetimes are 4.49 and 4.21 ns at 298 K.[76] The authors indicated that this emission was fluorescence arising from the ligands and that the ligand was uncoupled to the Re atom when coordinated, but the 8–9 nm red shift of the emission bands upon complexation clearly suggests otherwise. These photophysical properties can be used as primary guidelines for assignments (fs < τ_F < 1 ps; 1 ps < τ_P < 2 ns at 298 K), but the τ_F data for **L6** (Table 1) also indicate that τ_F can reach the ns-time scale.

The new complexes reported are found to be weakly or reasonably emissive respectively at 298 and 77 K. The absorption and emission spectra and photophysical data of **1a** and **1b** are provided in Fig. 7 and 8 and Tables 2 and 3, respectively, as representative examples (see ESI‡ for the other complexes; Fig. S23–S40‡). The steady state and time-resolved absorption and emission spectra are reminiscent to those for **L6** although these are somewhat red-shifted. This behaviour is consistent with ligand–Re interactions. The τ_e data are also similar to those of **L6**, although new components are now depicted by the Streak camera at 298 K (Table 2). These components resemble the τ_F data of free **L6** at 77 K, which is interpreted by an increase in molecular rigidity upon ligand chelation.

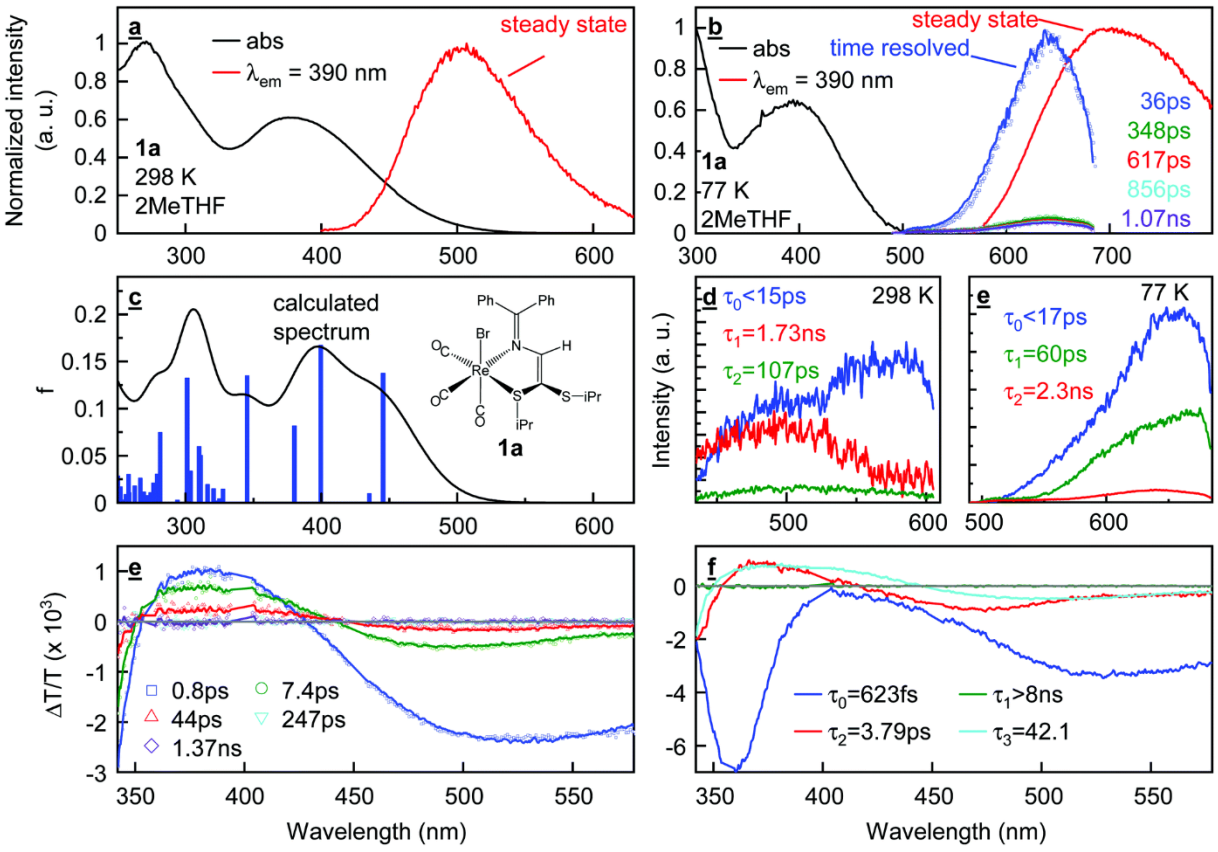

Fig. 7 a and b: Steady state absorption (black) and emission (red) spectra of **1a** in 2-MeTHF at 298 and 77 K, respectively. The time-resolved emission spectra of **1a** in 2-MeTHF (different colors) at 298 (frame d) and 77 K (frame e) are also shown. Note: The Streak camera spectra are uncorrected for the instrument response and the spectra of short-lived species (τ_F < IRF, blue traces) are severely distorted. c: Left; Simulated absorption spectrum of **1a** (TDDFT, applying a THF solvent field is applied); the bar graph (blue) reports the oscillator strengths (f) and positions of the 100st electronic transitions. An arbitrary thickness of 3000 cm^{-1} was assigned to each bar for the spectra simulation. d (298 K) and e (77 K): decay associated spectra of **1a** in

2-MeTHF (Streak camera; λ_{exc} = 397 nm, note that the spectra are not corrected for the PMT response). f: Time evolution of the fs-TAS of **1a** in 2-MeTHF at 298 K (λ_{exc} = 397 nm). The bleach and transient signals are positive and negative signals, respectively. The delay times are indicated. g: Decay associated spectra of the fs-TAS of **1a**. Note that no species decaying in the ns time scale are observed. Note that the positive and negative responses represent the bleached and transient signals, respectively.

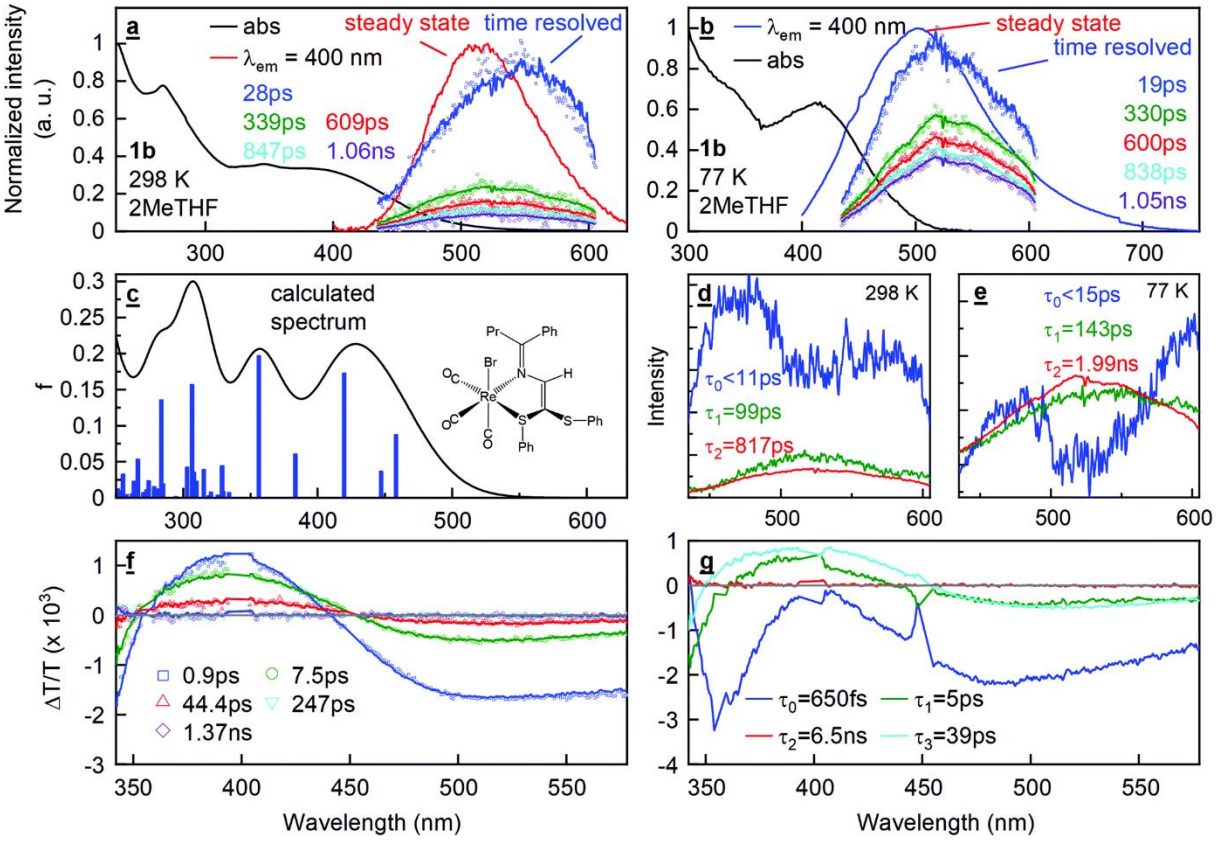

Fig. 8 a and b: Steady state absorption (black) and emission (red) spectra of **1b** in 2-MeTHF at 298 and 77 K, respectively. The time-resolved emission spectra of **1b** in 2-MeTHF (different colors) at 77 (frame d) and 298 K (frame e) are also shown. Note: The Streak camera spectra are uncorrected for the instrument response, and the spectra of short-lived species (τ_F < IRF) are severely distorted. c: Left; Simulated absorption spectrum of **1b** (TDDFT, applying a THF solvent field is applied); the bar graph (blue) reports the calculated oscillator strengths (f) and positions of the 100st electronic transitions. An arbitrary thickness of 3000 cm^{-1} is assigned to each bar for the spectra simulation. d (298 K) and e (77 K): DAS of **1b** in 2-MeTHF (Streak camera; λ_{exc} = 397 nm, note that the spectra are not corrected for the PMT response and the spectra of short-lived species (τ_F < IRF, blue traces) are severely distorted). f: Time evolution of the fs-TAS of **1b** in 2-MeTHF at 298 K (λ_{exc} = 397 nm). The bleach and transient signals are

positive and negative signals, respectively. The delay times are indicated. g: Decay associated spectra of the fs-TAS of **1b**. Note that no species decaying in the ns time scale are observed. Note that the positive and negative responses represent the bleached and transient signals, respectively.

Table 2 Emission (τ_e) and excited state (τ_e) lifetimes of **1a–j** in 2-MeTHF at 298 K

Complex (λ_{emi})	**τ_e (ps) (Streak)**			**τ_e (fs-TAS)[b]**
1a (507 nm)	<14[a]			623 fs, 3.8 ps, 42.1 ps
1b (514 nm)	<11[a]	100	820	651 fs, 5.0 ps, 39.2 ps
1c (523 nm)	<11[a]	135	1430	630 fs, 6.1 ps, 40.0 ps
1d (501 nm)	<16[a]	145		157 fs, 496 fs, 4.6 ps, 38.4 ps
1e (504 nm)	<9[a]	160	730	644 fs, 3.1 ps, 44.2 ps
1f (474 nm)	<11[a]	120	1500	163 fs, 373 fs, 4.1 ps, 33.8 ps
1g (467 nm)	<12[a]			128 fs, 524 fs, 4.9 ps, 30.3 ps
1h (469 nm)	<11[a]			671 fs, 5.3 ps, 34.2 ps
1i (493 nm)	<12[a]	97	1880	459 fs, 12.3 ps, 265 ps
1j (490 nm)	<13[a]	110	650	684 fs, 27.3 ps

a Very weak signal (τ_F) and the decays are within the IRF. The Streak camera is better suited to measure lifetimes in the ps –~2 ns window. Note that the emission intensity of the complexes at this temperature is too weak to be analyzed by TCSPC. b Note that the complexes are sufficiently emissive enough at 298 K for TCSPC analysis due to the low power of the LED laser.

Table 3 Emission Lifetimes (τ_e) of **1a-j** in 2-MeTHF at 77 K

Complex (steady state λ_{emi})	**τ_F (ps) Streak[b]**	**τ_F (ps) Streak[b]**	**B_i[a]**	**τ_F; ns (*f*; %) TCSPC[b]**	**B_i[a]**	**τ_P; ns (*f*; %) TCSPC[b]**	**χ^2**
1a (700 nm)	<17	60	0.0037	1.70 (24)	0.0019	5.34 (38)	1.051
1b (500 nm)	<15	143	0.0167	1.38 (41)	0.0062	4.60 (51)	1.003
1c (535 nm)	<16	160	0.0148	1.15 (42)	0.0039	4.09 (40)	1.038
1d (510 nm)	<16	146	0.0082	1.29 (22)	0.0062	4.70 (61)	1.061
1e (450 nm)	31	163	0.0472	1.85 (42)	0.0154	6.94 (52)	1.029
1f (535 nm)	<15	157	0.0041	1.76 (39)	0.0019	5.36 (53)	1.040
1g (540 nm)	<17	—	0.0052	1.92 (42)	0.0021	5.86 (54)	1.001
1h (520 nm)	17	131	0.0122	1.41 (42)	0.0031	5.22 (39)	1.000
1i (530 nm)	—	99	0.0096	1.68 (29)	0.0055	5.80 (57)	1.030

Complex (steady state λ_{emi})	τ_F (ps) Streak[b]	τ_F (ps) Streak[b]	B_i[a]	τ_F; ns (f; %) TCSPC[b]	B_i[a]	τ_P; ns (f; %) TCSPC[b]	χ^2
1j (640 nm)	<15	93	0.0080	1.40 (33)	0.0030	4.74 (42)	1.183

a $f_i(\%) = (B_i\tau_i)/\sum(B_i\tau_i)\cdot 100\%$; $I_e(t) = B_1\exp(-t/\tau_1) + B_2\exp(-t/\tau_2) + B_3\exp(-t/\tau_3) + \ldots$. b The Streak camera is suited to measure lifetimes in the ps–~2 ns window; TCSPC is better suited to extract lifetimes placed between ~100 ps (*i.e.* FWHM of laser pulse) and ~1 μs. Note that the sum of the f% values is not equal to 100% because the remainder is close to the lamp profile (*i.e.* approaching or smaller than 100 ps), and cannot be extracted accurately.

Importantly, the steady state spectra exhibit a strong signal at ~700 nm (instead of ~550 nm, Fig. 7b) spreading well in the near-IR region, which is not depicted by the Streak camera (upper detection limit = 2 ns). The subtraction of the fluorescence spectrum (Streak camera) from the steady state spectrum gives a resulting emission band profile with a maximum at ~740 nm (Fig. S41‡). In all es, the TCSPC measurements at 77 K indicate the presence of a new component ($4.1 < \tau_P < 6.9$ ns), which is absent in the free ligand. This new feature is readily assigned to a triplet emission. This time scale contrasts with that generally reported for the *fac*-halotricarbonyl(diimine)rhenium complexes (μs) at this same temperature,[52–59] and appears consistent with the fast and ultrafast radiative and non-radiative relaxation time scales depicted for the singlet excited states.

Strikingly, the heavy atom effect is barely perceptible upon comparing the TCSPC τ_F data at 77 K of **L6** (0.44 and 1.68 ns) with those of the complexes (Table 3; average values 0.13 and 1.54 ns). The attenuated decrease of τ_F upon complexation with Re(i) appears linked to the increase in skeleton rigidity. However, the τ_F and τ_P data do not follow the expected trend for heavy atom effect for X = Cl, Br and I, where the τ_F and τ_P values vary as Cl(**1c**) < Br(**1b**) < I(**1g**). This unexpected trend remains unexplained.

Singlet states

The nature of the S_1 states was addressed by examining the calculated frontier MOs (Fig. 9), and the positions and oscillator strengths of the lowest energy electronic transitions (Tables 4 and 5) for **1i** and **1j** as representative examples (see ESI‡ for the other complexes; Fig. S45–S89, Tables S10–S36‡). Using TD-DFT computations (Table 5), the two lowest energy electronic transitions (*i.e.* 0–0 component) are found in the vicinity of 450–463 nm and their major contributions to the transition are pure HOMO → LUMO for **1a** (also **1f**, **1h** and **1j**) and a mixture of HOMO → LUMO and HOMO−1 → LUMO for **1b** (also **1c**, **1g** and **1i**) for both

es. The MO representations (Fig. 9) and atomic contributions (Table 4) indicate that the HOMO−1 and HOMO are mostly located onto the [Re] unit ([Re] = *fac*-ReX(CO)$_3$ moiety), whereas the LUMO is mostly located on the Ph_2C=N–HC=C(S)$_2$ skeleton, reminiscent of that for the free ligand **L6**. Consequently, these two lowest singlet excited states are metal-to-ligand charge transfer (MLCT) where metal stands for [Re]. This conclusion is consistent with what is generally reported for the *fac*-halo(diimine)tricarbonlythenium(i) species.[71,72]

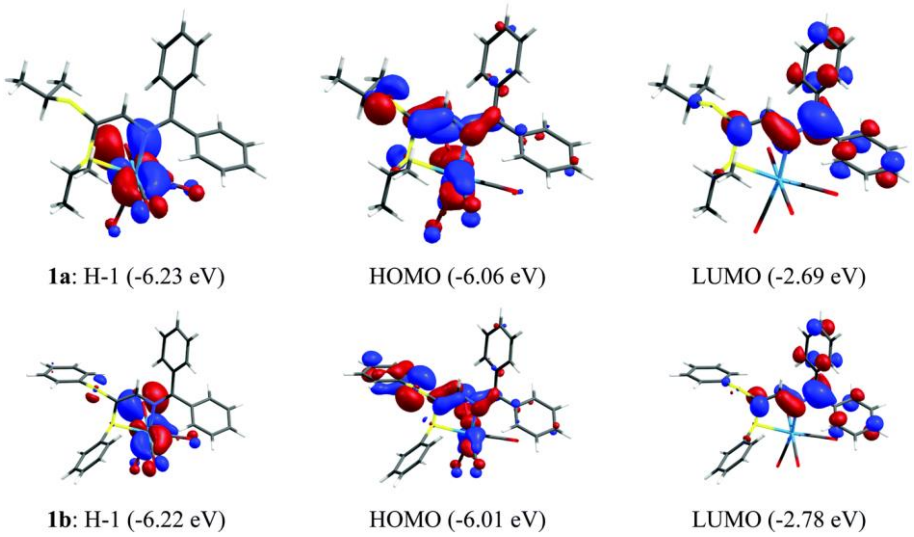

Fig. 9 Representations of the frontier MOs for **1a** and **1b** using the X-ray structures and THF as the solvent field. The energies are in eV. For the other MOs, see the ESI‡ (H = HOMO).

Table 4 Relative atomic contributions (%) of the various fragments of the frontier MOs of **1a** and **1b**[a]

Complex, MO	Re	CO	X	S^N ligand
1a, HOMO−1	38%	17%	39%	6%
1a, HOMO	20%	10%	16%	54%
1a, LUMO	2%	2%	0%	95%
1b, HOMO−1	35%	16%	37%	12%
1b, HOMO	13%	6%	8%	73%
1b, LUMO	2%	2%	0%	96%

a See ESI‡ for more frontier MOs and for the data for the other complexes; a THF solvent field is applied.

Table 5 Calculated positions, oscillator strengths (*f*) and major contributions (%) of the first singlet–singlet electronic transitions for **1a** and **1b** (H = HOMO)[a]

Complex	No.	λ (nm)	f	Major contributions (%)
1a	1	446.2	0.1361	HOMO → LUMO (86)
	2	436.9	0.0167	H−1 → LUMO (92)
1b	1	462.2	0.1198	H−1 → LUMO (29), HOMO → LUMO (68)
	2	450.1	0.0629	H−2 → LUMO (27), H−1 → LUMO (56), HOMO → LUMO (16)

a See ESI‡ for more frontier MOs and for the data for the other complexes; a THF solvent field is applied.

In this series, DFT and TDDFT analysis demonstrated that intraligand charge-transfer (ILCT) excited states along with mixed versions ILCT/MLCT are also possible. Table 6 compares the nature of the frontier MOs and lowest energy spin allowed electronic transitions. First, the formation of both S_1 and S_2 states always occurs with the isolated LUMO exclusively (detail in the ESI‡). Second, regardless of the nature of the lowest energy electronic transition (ILCT, MLCT, or mixed ILCT/MLCT), the calculated positions of the 0–0 peaks are found in a narrow range (432–480 nm), which is consistent with the fact that the absorption and fluorescence bands are also found in the same range, with no obvious trend. Third, the LUMO is always located on the (S^N) ligand. This conclusion on the constant involvement of the imine–thioether ligand in the atomic contributions of the frontier MOs corroborates the fact that the excited states of the complexes are strongly influenced by the features presented by the ligand, as described above. This conclusion is also in line with the fact that the fluorescence bands appear in a similar spectral range as for the ligand and the multiple exponential decays are also observed for the complexes.

Table 6 Nature of the frontier MOs and lowest energy spin-allowed electronic transitions[a]

	1a	**1b**	**1c**	**1e**	**1f**	**1g**	**1h**	**1i**	**1j**
H−1	[Re]	[Re]	[Re]	[Re]	[Re]	[Re]	(S^N)	[Re]	Mixed
HOMO	Mixed	(S^N)	(S^N)	(S^N)	(S^N)	[Re]	(S^N)	[Re]	(S^N)
LUMO	(S^N)	(S^N)	(S^N)	(S^N)	(S^N)	(S^N)	(S^N)	(S^N)	(S^N)
S_1	Mixed	ILCT	ILCT	ILCT	ILCT	MLCT	ILCT	MLCT	ILCT
λ (nm)	446.2	462.2	460.0	440.6	483.7	479.9	441.7	449.8	463.9

	1a	1b	1c	1e	1f	1g	1h	1i	1j
S_2	Mixed	Mixed	Mixed	Mixed	Mixed	MLCT	ILCT	MLCT	MLCT
λ (nm)	436.9	450.1	443.5	431.5	461.3	472.4	421.8	436.9	410.6

a H−1 = HOMO−1, [Re] = *fac*-Re(CO)$_3$X, mixed = ILCT/MLCT.

Triplet states

The nature of the lowest energy triplet excited states was also addressed by DFT computations by examining the atomic contributions of the lowest and highest singly occupied MOs of the complexes, LSOMO and HSOMO (Fig. 10 and Table 7 for **1a** and **1b**, see ESI of the other complexes). For both complexes, the atomic contributions of the HSOMO are the largest in the (S^N) ligand, namely on the Ph_2C=N moiety. Conversely, the atomic contributions of the LSOMO is almost evenly distributed over both the [Re] and ligand (*i.e.* mostly C=N–CH=C). So, the triplet excited state built upon the LSOMO and HSOMO has a mixed nature, MLCT/ILCT. Concurrently, the LSOMO−1 exhibits atomic contributions located on the [Re] unit meaning that an upper triplet excited state built upon LSOMO−1 and HSOMO would be MLCT.

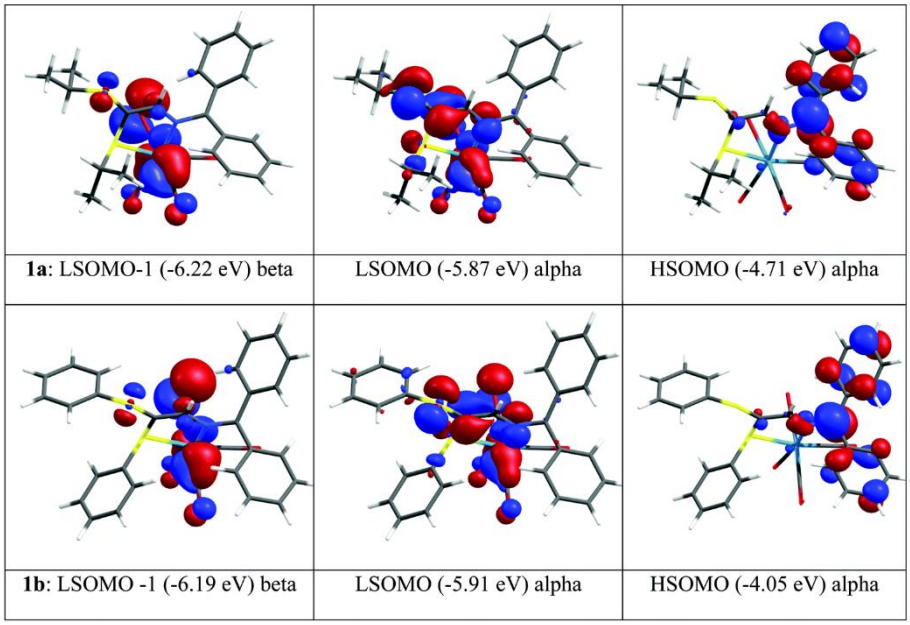

Fig. 10 Representations of the singly occupied frontier MOs for **1a** and **1b** (solvent field = THF).

Table 7 Relative atomic contributions (%) of the various fragments to the singly occupied MOs of **1a** and **1b** (see the ESI‡ for the other complexes)[a]

1a; fragments	**LS−1**	**LSOMO**	**HSOMO**	**HS+1**
Re	**37%**	19%	2%	5%
3(CO)	16%	9%	2%	4%
Br	32%	10%	0%	2%
N–S_ligand	15%	**62%**	**95%**	**89%**

1b; fragments	**LS−1**	**LSOMO**	**HSOMO**	**HS+1**
Re	**36%**	20%	2%	5%
3(CO)	15%	9%	2%	4%
Br	33%	10%	0%	2%
N–S_ligand	16%	**60%**	**95%**	**89%**

a HS = HSOMO, LS = LSOMO; the values in bold represent the major contributions.

Table 8 compares the nature of the singly occupied frontier MOs and of the lowest triplet excited states of all the complexes. These computational results are expectedly reminiscent to that for the singlet excited states (Table 6), and the conclusion is that the emissive states can be MLCT, ILCT or a mixture MLCT/ILCT. The comparison between **1j** → **1c** → **1b** → **1g** (respectively X = OTf, Cl, Br, I), indicates that the computed nature of the T_1 state evolves respectively from ILCT → ILCT → mixed ILCT/MLCT → MLCT. The comparison between **1c**, **1f** and **1h** (X = Cl) indicates that T_1 is ILCT for all three es. The calculated difference between the energy of the LSOMO (LS) and LSOMO−1 (LS−1) should qualitatively represent the T_2–T_1 gap (Δ) as well. These calculated Δ's range are from 970 to 4110 cm^{-1}, averaging 2570 cm^{-1}, and suggest that T_1 must be well isolated in energy from T_2.

Table 8 Nature of the semi-occupied frontier MOs and of the lowest triplet excited states[a]

	1a	**1b**	**1c**	**1e**	**1f**	**1g**	**1h**	**1i**	**1j**
LS−1	[Re]	[Re]	[Re]	[Re]	[Re]	[Re]	[Re]	[Re]	[Re]
E (eV)	−6.22	−6.19	−6.26	−6.28	−6.30	−6.03	−6.24	−6.17	−6.61
LS	Both	Both	(S^N)	(S^N)	(S^N)	Both	(S^N)	Both	(S^N)
E (eV)	−5.87	−5.91	−5.94	−5.90	−5.93	−5.86	−5.87	−5.974	−6.10
HS	(S^N)	(S^N)	(S^N)	(S^N)	(S^N)	(S^N)	(S^N)	(S^N)	(S^N)
E (eV)	−4.71	−4.05	−4.72	−4.72	−4.91	−4.72	−4.72	−4.76	−4.80
HS+1	(S^N)	(S^N)	(S^N)	(S^N)	(S^N)	(S^N)	(S^N)	(S^N)	both
E (eV)	−3.96	−4.05	−4.04	−3.91	−4.10	−4.07	−3.92	−4.09	−4.13

	1a	1b	1c	1e	1f	1g	1h	1i	1j
T_1	Mixed	Mixed	ILCT	ILCT	ILCT	Mixed	ILCT	Mixed	ILCT
T_2	MLCT	MLCT	MLCT	MLCT	MLCT	Mixed	ILCT	Mixed	Mixed
Δ (cm^{-1})	2820	2260	2580	3060	2980	1370	2980	970	4110

a LS = LSOMO, HS = HSOMO, [Re] = *fac*-$Re(CO)_3X$, both = [Re] and (S^N) (the detail of the atomic contributions for each singly occupied MOs are placed in the ESI,‡ mixed = ILCT/MLCT, $T_1 = {}^1LS/{}^1HS$, $T_2 = {}^1LS{-}1/{}^1HS$, $\Delta = E(LS) - E(LS{-}1)$, which may be similar to the T_2–T_1 energy gap. Note that HS+1 is too high in energy to be involved in the formation of a low-lying triplet state.

Singlet oxygen

The near-IR region was examined to see whether singlet oxygen was produced in air-saturated solution (the phosphorescence band is generally located at ~1270 nm), but this zone was completely silent. This observation is fully consistent with the fact that at room temperature the excited state lifetimes of the complexes, regardless they are singlet or triplet states, are too short-lived to promote the diffusion controlled bimolecular energy transfer processes (Table 2), the longest one being only 1.88 ns (**1h**). It is interesting to mention that the free $Ph_2C{=}N{-}CH{=}C(SPh)_2$ ligand can be oxidatively photocleaved in the presence of singlet oxygen, but no photodecomposition of the complexes was observed during the near-IR screening.[68] The overall investigations of the photophysical properties and DFT computations are summarized in Fig. 11.

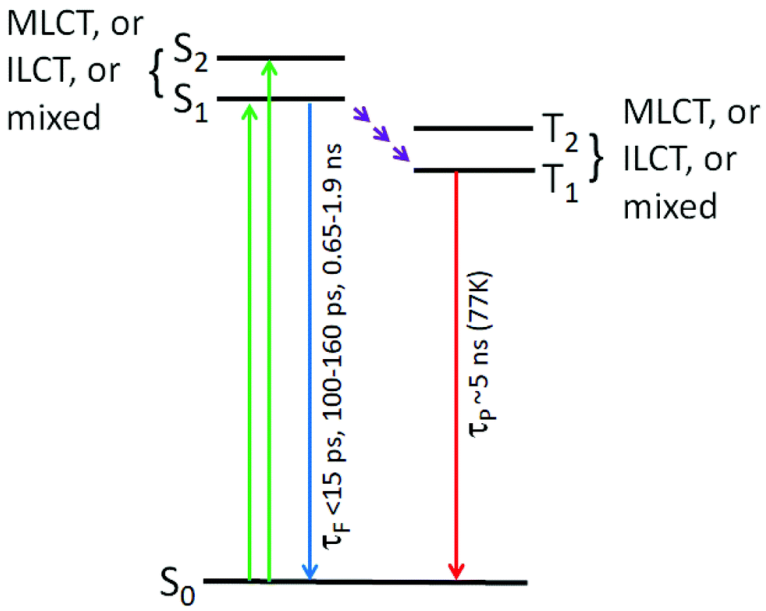

Fig. 11 State diagram summarizing the photophysical properties of the rhenium complexes.

Electrochemical study

The redox properties of the *fac*-halotricarbonyl(S^N)rhenium(i) complexes and **L2** and **L6** have been investigated by cyclic voltammetry (CV) in CH_2Cl_2 solutions in the −2.30/+1.50 V (*vs.* Ag/$AgClO_4$) range. CV measurements have also been conducted for some samples in MeCN in order to address the influence of a coordinating solvent. Beside shifts of peak potentials, no significant changes have been observed in the voltamograms. The CV data are summarized in Table 9. A reasonable agreement was found between computed and measured HOMO–LUMO gaps.

Table 9 Redox potentials of *fac*-halotricarbonyl(S^N)rhenium(i) complexes (in V *vs.* Ag/$AgClO_4$)

	Reduction		**Oxidation**	E_g **(eV)**	
Compound	E^{pa}	$E^{1/2}$	E^{pa} **or** $E^{1/2(*)}$	$E^{electrochemistry}_g$	E^{comput}_g **(2-MeTHF)**
L2 (CH_3CN)	−1.99	—	0.73	2.72	—
L2 (CH_2Cl_2)	−2.19	—	0.88	3.07	—
L6 (CH_2Cl_2)	−2.00	—	0.92	2.92	3.43
1a (CH_3CN)	−1.98	−1.34	1.15	3.13	3.38
1a (CH_2Cl_2)	−2.08	−1.41	1.35	3.43	
1b (CH_3CN)	−1.87	−1.21	1.17	3.04	3.27
1b (CH_2Cl_2)	−1.97	−1.27	1.28	3.25	
1c (CH_2Cl2)	−1.96	−1.26	1.20[b]	3.16	3.26
1d (CH_2Cl_2)	−1.91	−1.26	1.18[b]	3.09	—
1e (CH_2Cl_2)	−2.03	−1.41	1.30	3.33	3.40
1g (CH_2Cl_2)	−1.86	−1.22	1.05	2.91	3.23
1h (CH_2Cl_2)	−1.86	−1.21	1.19[b]	3.05	3.31

a Potential peak at a scan rate of 100 mV s^{-1}. b Observed at a scan rate of 1 V s^{-1}.

All complexes display one reversible reduction wave in the −1.21 V to −1.41 V range. The most negative reduction waves are observed for complexes **1a** and **1e**, which bear electrodonating thioethers. Thus a S^N ligand-centred reduction is assigned for this process, which is also consistent with the reported electrochemical studies on [$Re(CO)_3$(N^N)X] complexes.[77] This assignment is also in line with the conclusions drawn from the DFT computations. At more negative potentials, an irreversible reduction wave between −1.86 and −2.08 V, is also depicted. Concurrently, the [$Re(CO)_3$(S^N)X] complexes are oxidized at potentials ranging from +1.05

to +1.35 V. The stability of the generated 17-electron species $[Re(CO)_3(S^N)X]^{\cdot+}$ varies with the nature of the ligands. At scan rate of 100 mV s^{-1}, the CVs show irreversible oxidation waves for all complexes, but at scan rates above 1 V s^{-1}, chemical reversibility for complexes **1c**, **1d** and **1h** was achieved (Fig. S90 and S91‡). Computational studies above indicate that the nature of the HOMO varies as [Re] for **1a**, **1b**, **1g**, and **1i**, (S^N) for **1c**, **1f**, **1h**, and **1j**, mixed [Re]/(S^N) for **1e**, and **1d** was not computed due to the absence of X-ray data (Table 6). The common point is that **1c** and **1h** exhibit a HOMO centred on the (S^N) ligand suggesting that the stability of the radical species may be associated with the HOMO being mainly located on the S^N ligand with a very small contribution from the halide. Noteworthy, it is generally accepted that in the $[Re(CO)_3(N^N)X]$ complexes, the irreversibility of the oxidation wave is due to the dissociation of halide.[67,77] We conclude that the Re–X bond may be less weakened after oxidation of the complexes **1a–1j**.

Concluding remarks

In summary, a series of diaryl-2-azabutadiene ligands (**L1–L6**) containing two thioether arms at the 4,3- or 4,4-positions were designed for their subsequent chelation onto a rhenium(i) center through the imine and one of the thioether groups, were performed to produce a new class of luminescent *fac*-$Re(N^S)(CO)_3X$ complexes, **1a–1j** (N^S = **L1–L6**). Generally, the modulation of the photophysical properties and kinetic parameters in the homologous diimine Re complexes is readily achieved upon changing X and the basic structure of the diimine chelate.[58] However, this modulation is not straightforward in this current series as the excited state lifetimes turned out to be very similar to each other between complexes (Tables 2 and 3), but also with respect to those of the ligand, leading to the unprecedented conclusion that the photophysical properties for this class of complexes are heavily governed by the structural traits of the unusual ligands.

The presence of the pendant thioether arm makes these tritopic species a new type of ligands where the chelating centre is an imine thioether frame, which structurally differs from the diimine chelates exhibiting dangling thioether residues.[76,78–80] Mono- and dithioether-containing organic ligands are commonly prone to construct 1D-,[81] 2D-[82] and 3D-[83] coordination polymers (CPs), ocionally found porous, with CuX salts (Cu = Cl, Br, I, CN), a metal(i) ion that is largely employed for this purpose. Concurrently, the number of examples of mono- and dithioether-containing organometallic counterparts, namely built with platinum(ii), is rather limited. Nonetheless they also form strongly luminescent 1D- and 2D- and even 3D CPs with CuX salts.[84–87] For species containing rhenium(i), an organometallic tetratopic ligand

$Ge(CH_2SPh)_4$, [Ge], which is known to generate luminescent CPs with CuI and $HgBr_2$,[88] was also used to prepare the organometallic complex *fac*-Re(**[Ge]**)$(CO)_3Br$, which bears two dangling CH_2SPh arms.[88] Concurrently, the $[Si(Me_2)_2(CH_2SPh)_2]_2$ ligand, **[Si–Si]**, forms a large bimetallic [*fac*-$Re(CO)_3Br$(**[Si–Si]**)]$_2$ metallacycle, but no CP material was isolated.[89]

In order to improve the two features mentioned above (*i.e.* high flexibility of the ligands (leading to short-lived excited states and low modulation of the photophysical properties with the X groups) and difficulty to obtain crystals suitable for X-ray crystallography during ligand and CP preparations), alternative ligand structures are possible. For instance, the rigidification and symmetrisation of the diaryl-2-azabutadiene-4,4-dithioether ligands is possible by simply substituting the $=C(SR)_2$ moieties (R = alkane chain) by the cyclic $=C(S(CH_2)_nS)$ groups (n = 4, 5).[90] These $Ph_2C=N–CH=C(S(CH_2)_nS)$ species (n = 4, 5), have apparently not been exploited in coordination chemistry. In the light of this work, these species deserve further consideration. The presence of a second dangling SR group, which is prone to coordinate other soft metal ions such as Cu(i) or Ag(i), offers the possibility to design innovative heterodinuclear species with targeted architectures allowing for the modulation of both redox and photophysical properties of new materials resulting from this family of Re(i)(S^N) synthons. We have also demonstrated that 2-azabutadies bearing two NR_2 groups at the instead of two thioether functions are synthetically accessible.[43] For example, the coordination of the piperidino-functionalized ligand $[Ph_2C=N–C(H)=C(NC_5H_{10})_2]$ and the exploration of its electrochemical and photophysical properties of this ligand on a $Re(CO)_3X$ motif would constitute an interesting topic for future work.

Experimental section

Apparatus and electrochemical set-up

The NMR spectra were recorded on a Bruker Avance 300 apparatus (300.13 and 75.1 MHz for ^1H and ^{13}C) in $CDCl_3$, unless otherwise stated. FT-IR analysis was performed on a Shimadzu IR Affinity-1 apparatus (CH_2Cl_2, ν in cm^{-1}). UV-vis spectra were measured with a VARIAN-Cary 100 spectrophotometer in CH_2Cl_2 at room temperature, the concentrations of the solutions are around 10^{-5} mol l^{-1}, λ_{max} in nm (ε in M^{-1} cm^{-1}). Mass spectra were obtained on an APCI-Q-TOF (maXis) system. Voltammetric analyses were carried out in a standard three electrode cell with a Radiometer PGP 201 potentiostat at ambient temperature. The electrolyte consisted of 0.2 M Bu_4NPF_6 solution in deaerated MeCN or CH_2Cl_2. The working electrode was a platinum disk electrode, and the auxiliary electrode was a platinum wire. The reference electrode was a

silver–silver ion electrode, Ag/Ag + (0.1 M $AgClO_4$ in MeCN) separated from the analysed solution by a sintered glass disk. After each measurement, the reference was checked against the ferrocene–ferriconium couple (+0.025 V and +0.16 V against this reference electrode in MeCN and in CH_2Cl_2 solution respectively.

Reagents

$[Re(\mu\text{-}Br)(CO)_3THF]_2$ [91] was prepared according to the literature procedure by refluxing $[ReBr(CO)_5]$ in THF, and $[ReI(CO)_5]$ was synthetized by oxidative cleavage of $[Re_2(CO)_{10}]$ in the presence of I_2.[92] $[ReCl(CO)_5]$ was purchased from STREM. Dichloromethane, MeCN, chloroform and dimethylformamide were dried over suitable reagents and freshly distilled under argon before use. All reactions were carried out by using standard Schlenk-tube techniques.

Synthetic procedures

4,4-Bis(naphtylthio)-1,1-diphenyl-2-azabuta-1,3-diene (L6)

2 mmol of 1,1-diphenyl-4,4-dichloro-2-azabuta-1,3-diene prepared according to the literature procedure[93] was stirred with an excess of sodium 2-naphtholate (10 mmol) in dry DMF (10 mL). The reaction mixture was stored at room temperature for 6 h, then poured into water (100 mL) and extracted with diethyl ether (3 × 50 mL). The organic solution was washed three times with water, dried over anhydrous sodium sulfate and evaporated. The crude residue was recrystallized from ethanol affording yellow needles yield: 78%. Mp = 127 °C. Anal. calcd for $C_{35}H_{25}NS_2$ C 80.27; H 4.81; N 2.67; S 12.25. Found: C 79.94; H 4.68; N 2.52; S 11.96. IR (KBr): ν(C=C): 1601, ν(C=N): 1574 cm^{-1}. ^1H NMR: δ/ppm 7.09–7.11 (m, 2H, *H*ar), 7.17 (s, 1H, *H*C=C), 7.25–7.43 (m, 14H, *H*ar), 7.50–7.90 (m, 8H, *H*ar). $^{13}C\{^1H\}$ NMR: δ/ppm 125.7–127.4 (18s, *C*ar), 129.1 (s, HC=*C*), 142.1 (s, *C*H=C), 166.8 (s, *C*=N). UV-vis: 232 (23 300), 252 (15 100), 383 (4100). MS ($APCI^+$) *m*/*z* 523.14 $[M]^+$.

Synthesis of complexes 1a–b, 1d and 1i

To a solution of $[Re(\mu\text{-}Br)(CO)_3THF]_2$ (211 mg, 0.25 mmol) in 8 mL of dichloromethane, the ligand (0.5 mmol) was added in several portions. The reaction mixture was stirred at room temperature for 1 h and then concentrated to *ca.* 4 mL under reduced pressure. Layering with heptane gave after several days at 5 °C red needles.

Synthesis of complexes 1c, 1e–f

$ReCl(CO)_5$ (361 mg, 1 mmol) and ligand **L1–7** (1.1 mmol) in $CHCl_3$ (8 mL) were heated at 50 °C for 3 h. After cooling of the reaction mixture to room temperature and concentration to *ca.* 4 mL under reduced pressure, layering with heptane afforded after several days at 5 °C red needles.

Synthesis of complex 1g

$ReI(CO)_5$ (227 mg, 0.5 mmol) and ligand **L2** (0.55 mmol) in $CHCl_3$ (6 mL) were heated at 55 °C for 3 h. After cooling of the reaction mixture to room temperature and concentration to *ca.* 4 mL under reduced pressure, layering with heptane afforded after several days deep red needles. X-ray suitable single-crystals were obtained by recrystallisation of a sample from CH_2Cl_2/heptane.

fac-[ReBr(CO)$_3${(Ph$_2$C=N–CH=C(S-iPr)$_2$}] (1a)

Yield: 70%. Anal. calcd for $C_{24}H_{25}BrNO_3ReS_2$ C, 40.85; H, 3.57; N, 1.98; S, 9.08. Found: C, 40.63; H, 3.49; N, 1.91; S, 8.98. IR: ν(CO): 2031vs, 1937s, 1898s cm^{-1}. ^1H NMR: δ/ppm 1.7 (d, 6H, ^3J = 6.7 Hz, CH(CH_3)$_2$), 1.57 (d, 6H, ^3J = 6.7 Hz, CH(CH_3)$_2$), 3.41–3.54 (sept, 1H, ^3J = 6.7 Hz, CH(CH$_3$)$_2$), 3.77–3.86 (sept, 1H, ^3J = 6.7 Hz, CH(CH$_3$)$_2$), 7.43–7.55 (m, 11H, *H*ar + *H*C=C). $^{13}C\{^1H\}$ NMR: δ/ppm 20.9–24.4 (4s, *C*H$_3$), 39.5–44.6 (2s, *C*H), 128.9 (s, HC=*C*), 131.9–137.4 (5s, *C*ar), 142.6 (s, *C*H=C), 154.0 (s, *C*=N), 187.3 (s, *C*O), 189.4 (s, *C*O), 192.6 (s, *C*O). MS (APCI$^+$) *m*/*z* 702.99 $[M]^+$.

fac-[ReBr(CO)$_3${(Ph$_2$C=N–CH=C(SPh)$_2$}] (1b)

Yield: 80%. Anal. calcd for $C_{30}H_{21}BrNO_3ReS_2$ C, 46.57; H, 2.74; N, 1.81; S, 8.28. Found: C, 46.49; H, 2.63; N, 1.77; S, 8.11. IR: ν(CO): 2033vs, 1938s, 1905s cm^{-1}. ^1H NMR: δ/ppm 7.29–7.34 (m, 6H, *H*ar + *H*C=C), 7.41–7.75 (m, 15H, *H*ar). $^{13}C\{^1H\}$ NMR: δ/ppm 128.4 (s, HC=*C*), 129.0–137.4 (17s, *C*ar), 142.6 (s, *C*H=C), 152.8 (s, *C*=N), 188.2 (s, *C*O), 189.8 (s, *C*O), 191.8 (s, *C*O). MS (APCI$^+$) *m*/*z* 770.96 $[M]^+$.

fac-[ReCl(CO)$_3${(Ph$_2$C=N–CH=C(SPh)$_2$}] (1c)

Yield: 75%. Anal. calcd for $C_{30}H_{21}ClNO_3ReS_2$ C, 49.41; H, 2.90; N, 1.92; S, 8.79. Found: C, 49.33; H, 2.79; N, 1.86; S, 8.69. IR: ν(CO): 2034vs, 1940s, 1903s cm^{-1}. ^1H NMR: δ/ppm 7.2–7.34 (m, 6H, *H*ar + *H*C=C), 7.42–7.74 (m, 15H, *H*ar). $^{13}C\{^1H\}$ NMR: δ/ppm 128.3 (s, HC=*C*), 128.4–137.5 (20s, *C*ar), 142.3 (s, *C*H=C), 152.6 (s, *C*=N), 188.1 (s, *C*O), 190.2 (s, *C*O), 192.8 (s, *C*O). MS (APCI$^+$) *m*/*z* 727.01 $[M]^+$.

fac-[ReBr(CO)$_3${(Ph$_2$C=N–CH=C(S-pTol)$_2$}] (1d)

Yield: 65%. Anal. calcd for $C_{32}H_{25}BrNO_3ReS_2$ C, 47.97; H, 3.14; N, 1.75; S, 7.99. Found: C, 47.85; H, 3.01; N, 1.68; S, 7.85. IR: ν(CO): 2031vs, 1937s, 1904s cm^{-1}. ^{1}H NMR: δ/ppm 2.34 (s, 3H, CH_3), 2.43 (s, 3H, CH_3), 7.11–7.64 (m, 19H, *H*ar + *H*C=C). ^{13}C{^{1}H} NMR: δ/ppm 21.3 (s, *C*H$_3$), 21.5 (s, *C*H$_3$), 128.1 (s, HC=*C*), 129.0–141.0 (15s, *C*ar), 142.7 (s, *C*H=C), 151.3 (s, *C*=N), 187.4 (s, *C*O), 189.9 (s, *C*O), 192.6 (s, *C*O). MS (APCI$^+$) *m*/*z* 798.99 [M]$^+$.

***fac*-[ReCl(CO)$_3${(Ph$_2$C=N–CH=C(S-*n*Bu)$_2$}] (1e)**

Yield: 75%. Anal. calcd for $C_{26}H_{29}ClNO_3ReS_2$ C, 45.30; H, 4.24; N, 2.03; S, 9.30. Found: C, 45.34; H, 4.29; N, 2.06; S, 9.34. IR: ν(CO): 2032vs, 1939s, 1899s cm^{-1}. ^{1}H NMR: δ/ppm 0.94 (t, 3H, ^3J = 6.4 Hz, CH_3), 1.02 (t, 3H, ^3J = 6.4 Hz, CH_3), 1.36–1.91 (m, 4H, 2CH_2), 2.63–3.19 (m, 4H, 2CH_2), 3.54 (t, 2H, ^3J = 6.4 Hz, SCH'_2), 4.05 (t, 2H, ^3J = 6.4 Hz, SCH'_2), 7.43–7.60 (m, 11H, *H*ar + *H*C=C). ^{13}C{^{1}H} NMR: δ/ppm 13.4 (s, *C*H$_3$),13.5 (s, *C*H$_3$), 21.6 (s, *C*H$_2$), 21.8 (s, *C*H$_2$), 29.8 (s, *C*H$_2$), 31.2 (s, *C*H$_2$), 34.3 (s, S*C*H$_2$), 42.5 (s, S*C*H$_2$), 128.0 (s, CH=*C*), 128.9–137.6 (10s, *C*ar), 142.5 (s, *C*H=C), 151.1 (s, *C*=N), 186.7 (s, *C*O), 189.9 (s, *C*O), 193.2 (s, *C*O). MS (APCI$^+$) *m*/*z* 687.08 [M]$^+$.

fac-[ReCl(CO)$_3${(pClPh)$_2$C=N–CH=C(S-pTol)$_2$}] (1f)

Yield: 82%. Anal. calcd for $C_{32}H_{23}Cl_3NO_3ReS_2$ C, 46.52; H, 2.81; N, 1.70; S, 7.76. Found: C, 46.41; H, 2.76; N, 1.67; S, 7.65. IR: ν(CO): 2033vs, 1942s, 1904s cm^{-1}. ^{1}H NMR: δ/ppm 2.35 (s, 3H, CH_3), 2.43 (s, 3H, CH_3), 7.11–7.63 (m, 17H, *H*ar + *H*C=C). ^{13}C{^{1}H} NMR: δ/ppm 21.3 (s, *C*H$_3$), 21.5 (s, *C*H$_3$), 127.9 (s, HC=*C*), 129.9–141.0 (10s, *C*ar), 143.0 (s, *C*H=C), 151.4 (s, *C*=N), 187.1 (s, *C*O), 189.3 (s, *C*O), 192.2 (s, *C*O).

fac-[ReI(CO)$_3${(Ph$_2$C=N–CH=C(SPh)$_2$}] (1g)

Yield: 67%. Anal. calcd for $C_{30}H_{21}INO_3ReS_2$ C, 43.90; H, 2.58; N, 1.71; S, 7.81. Found: C, 43.79; H, 2.44; N, 1.65; S, 7.74. IR: ν(CO): 2032vs, 1937s, 1906s cm^{-1}. ^{1}H NMR: δ/ppm 7.31–7.73 (m, 21H, *H*ar + *H*C=C). ^{13}C{^{1}H} NMR: δ/ppm 128.5 (s, HC=*C*), 129.0–137.2 (11s, *C*ar), 142.9 (s, *C*H=C), 152.8 (s, *C*=N), 187.9 (s, *C*O), 188.9 (s, *C*O), 192.0 (s, *C*O). MS (APCI$^+$) *m*/*z* 818.95 [M]$^+$.

fac-[ReCl(CO)$_3${(Ph$_2$C=N–CH=C(S-naphthyl)$_2$}] (1h)

Yield: 78%. Anal. calcd for $C_{38}H_{25}ClNO_3ReS_2$ C, 55.03; H, 3.04; N, 1.69; S, 7.73. Found: C, 54.96; H, 2.97; N, 1.62; S, 7.66. IR: ν(CO): 2034vs, 1942s, 1904s cm^{-1}. ^{1}H NMR: δ/ppm 7.29–

7.41 (m, 6H, *H*ar + *H*CC), 7.43–7.58 (m, 16H, *H*ar), 7.66–7.95 (m, 16H, *H*ar). $^{13}C\{^{1}H\}$ NMR: *δ*/ppm 126.9 (s, HC*C*), 127.0–137.4 (19s, *C*ar), 142.3 (s, *C*HC), 152.8 (s, *C*=N), 188.3 (s, *C*O), 190.3 (s, *C*O), 192.3 (s, *C*O). MS (APCI^{+}) *m*/*z* 827.05 $[M]^{+}$.

fac-[ReBr(CO)$_3${(Ph$_2$C=N–C(S-tBu)=CH(S-tBu)}] (1i)

Yield: 75%. Anal. calcd for $C_{26}H_{29}BrNO_3ReS_2$ C, 42.56; H, 3.98; N, 1.91; S, 8.74. Found: C, 42.44; H, 3.89; N, 1.86; S, 8.67. IR: *ν*(CO): 2031vs, 1936s, 1899s cm^{-1}. ^{1}H NMR: *δ*/ppm 1.49 (s, 9H, –C(C*H*$_3$)$_3$), 1.66 (s, 9H, –C(C*H*$_3$)$_3$), 6.90 (s, 1H, C=C*H*), 7.28–7.64 (m, 10H, Ar–*H*). $^{13}C\{^{1}H\}$ NMR: *δ*/ppm 28.6–31.6 (6s, C(*C*H$_3$)$_3$), 49.6 (s, *C*(CH$_3$)$_3$), 55.7 (s, *C*(CH$_3$)$_3$), 128.4–142.2 (2s, CH=*C* + *C*ar), 145.3 (s, N–*C*), 153.9 (s, *C*=N), 189.7 (s, *C*O), 191.1 (s, *C*O), 193.2 (s, *C*O).

fac-[ReOTf(CO)$_3${(Ph$_2$C=N–CH=C(SPh)$_2$}] (1j)

[ReCl(CO)$_3${(Ph$_2$CN–CHC(SPh)$_2$}] (**1c**) (300 mg, 0.38 mmol) and AgOTf (100 mg, 0.389 mmol) were stirred in 20 mL in CH_2Cl_2 at room temperature overnight. After filtration, the solvent volume was reduced to *ca.* 4 mL. Layering the orange solution with hexane gave after one day at −20 °C orange needles. Yield: 87%. Anal. calcd for $C_{31}H_{21}F_3NO_6ReS_3$ C, 44.17; H, 2.51; N, 1.66; S, 11.41. Found: C, 44.05; H, 2.46; N, 1.61; S, 11.34. IR: *ν*(CO): 2044vs, 1952s, 1920s. ^{1}H NMR: *δ*/ppm 7.14–7.25 (m, 7H, *H*ar + *H*C=C), 7.34–7.58 (m, 12H, *H*ar), 7.70–7.81 (m, 2H, *H*ar). $^{13}C\{^{1}H\}$ NMR: *δ*/ppm 118.9 (q, $^{1}J_{C-F}$ = 319 Hz, *C*F$_3$)127.6 (s, HC=*C*), 128.3–137.6 (16s, *C*ar), 142.4 (s, *C*H=C), 149.4 (s, *C*=N), 188.0 (s, *C*O), 191.0 (s, *C*O), 193.2 (s, *C*O). MS (APCI^{+}) *m*/*z* 841 $[M]^{+}$.

Photophysical set-up

The absorption spectra in the solution were measured on a Varian Cary 300 Bio UV-vis spectrometer at 298 K and on a Hewlett-Packard 8452A diode array spectrometer with a 0.1 s integration time at 77 K. The steady state fluorescence spectra were acquired on an Edinburgh Instruments FLS980 phosphorimeter equipped with single monochromators. Fluorescence and phosphorescence lifetime measurements were made with the FLS908 spectrometer using a 395 nm pulsed diode laser as an excitation source. Data collection on the FLS980 system was performed using time correlated single photon counting (TCSPC). All fluorescence spectra were corrected for instrument response. All measurements at 77 K were performed with an EPR Dewar assembly using an NMR tube. The fluorescence lifetimes were extracted using multi-

exponential analyses. For time-resolved measurements, the concentrations were approx. 5×10^{-5} mol l^{-1} to match 0.4 in absorbance.

Femtosecond transient absorption spectroscopy (fs-TAS)

The fs transient spectra and decay profiles were acquired on a homemade system using the SHG of a Soltice (Spectra Physics) Ti-sapphire laser (λ_{exc} = 398 nm; fwhm = 75 fs; pulse energy = 0.1 μJ per pulse, rep. rate = 1 kHz; spot size ~500 μm), a white light continuum generated inside a sapphire window and a custom-made dual CCD camera of 64 × 1024 pixels sensitive between 200 and 1100 nm (S7030, Spectronic Devices). The delay line permitted to probe up to 4 ns with an accuracy of ~4 fs. The results were analysed with the program Glotaran (http://glotaran.org) permitting to extract a sum of independent exponentials that fits the whole 3D transient map.

Fast kinetic emission decay measurements

The laser source was the same as described above. The IRF increased to a FWHM of ~9 ps after passing through the optics at 298 K and become 12 ps after passing through a Dewar for 77 K measurements. The detector was a Streak Camera (Axis-TRS, Axis Photonique Inc.) limited to a maximum of ~2.5 ns. The results were globally analysed with the program Glotaran

(http://glotaran.org) permitting to extract a sum of independent exponentials . The resulting time-resolved spectra are not corrected for the instrument response.

Computations

The density functional theory (DFT) and time dependent density functional theory (TDDFT) calculations were performed with Gaussian 16[94] at the Université de Sherbrooke with the Mammoth supercomputer supported by *Le Réseau Québécois De Calculs Hautes Performances*. All cif files from X-ray crystal structures have been used for the calculations. The DFT (ground states) as well as TDDFT calculations[95–103] were carried out using the B3LYP method, triplet states were optimized using uB3LYP method. The 6-31g* basis set was used for C, H, N, O and S atoms.[103] The effective core potentials (ECP) and their associated double-ζ LANL2DZ basis set were used for all Re, Br, I, F and Cl atoms.[104–106] All calculations were carried out in a THF solvent field. No imaginary frequencies were observed validating the correct energy minimization after the optimization. The calculated absorption spectra were obtained from GaussSum 3.0.[107] Isosurfaces were generated with a contour value of 0.0432, red lobes are positive and blue lobes are negative.

Experimental X-ray crystallography

Suitable crystals were mounted on Nonius Kappa CCD (ligand **L6**, complexes **1b**, **1e-mono**, **1i**), Nonius Kappa ApexII (**1e-tricl**), **1f** and **1j**) and Bruker D8 VENTURE (**1a**, **1g**, **1h**) diffractometers. Crystal data as well as the information on data collections and structure solutions and refinements are summarized in Tables S5–S7 of the ESI.‡ The unit cells refinements, data reductions and scale corrections were performed using DENZO and SCALEPACK program.[108] The structures were solved either with SIR92,[109] SUPERFLIP[110] or SHELXT[111] direct methods. The multi-scan absorption correction of Blessing[112] or SADABS[113] was applied for complexes but not for the ligand **L6**. The models have been refined by least squares with SHELXL.[111] The non-hydrogen atoms were refined with anisotropic temperature factors. The hydrogen atoms were placed in calculated positions and isotropically refined using a riding model. There are the highly disordered solvent molecules in the structures of **1b** (heptane) and **1g** (CH_2Cl_2). The modelling of these disorders was unsuccessful and consequently, the SQEEZE utility in PLATON was applied. Olex2 has been used as graphical interface and for calculations of non-covalent distances and torsion and dihedral angles.[114]

Author contributions

All authors have read and agreed to the published version of the manuscript.

Conflicts of interest

There are no conflicts to declare.

Acknowledgements

PDH acknowledges the Natural Sciences and Engineering Research Council of Canada. CS thanks the Deutsche Forschungsgemeinschaft. MK, AK and MMK acknowledge the CNRS and Stéphanie Boullanger for her assistance for recording the NMR and IR spectra.

References

1. A. Coleman , C. Brennan , J. G. Vos and M. T. Pryce , *Coord. Chem. Rev.*, 2008, **252** , 2585 —2595.
2. A. Kumar , S. S. Sun and A. J. Lees , *Top. Organomet. Chem.*, 2010, **29** , 1 —35.
3. A. Vlček *Top. Organomet. Chem.*, 2010, **29** , 73 —114.

4. P. Lang , M. Pfrunder , G. Quach , B. Braun-Cula , E. G. Moore and M. Schwalbe , *Chem. – Eur. J.*, 2019, **25** , 4509 —4519.

5. S. A. Zav'yalov , I. A. Myasnikov and E. V. Karmanova , *Khim. Fiz.*, 1985, **4** , 989 —993.

6. S. K. Lee , M. Kondo , M. Okamura , T. Enomoto , G. Nakamura and S. Masaoka , *J. Am. Chem. Soc.*, 2018, **140** , 16899 —16903.

7. S. Yang , W. Hu , X. Zhang , P. He , B. Pattengale , C. Liu , M. Cendejas , I. Hermans , X. Zhang , J. Zhang and J. Huang , *J. Am. Chem. Soc.*, 2018, **140** , 14614 —14618.

8. J. S. Lee , D. Il Won , W. J. Jung , H. J. Son , C. Pac and S. O. Kang , *Angew. Chem., Int. Ed.*, 2017, **56** , 976 —980.

9. K. M. Choi , D. Kim , B. Rungtaweevoranit , C. A. Trickett , J. T. D. Barmanbek , A. S. Alshammari , P. Yang and O. M. Yaghi , *J. Am. Chem. Soc.*, 2017, **139** , 356 —362.

10. A. M. Potocny , J. J. Teesdale , A. Marangoz , G. P. A. Yap and J. Rosenthal , *Inorg. Chem.*, 2019, **58** , 5042 —5050.

11. R. M. Spada , M. Cepeda-Plaza , M. L. Gómez , G. Günther , P. Jaque , N. Pizarro , R. E. Palacios and A. Vega , *J. Phys. Chem. C*, 2015, **119** , 10148 —10159.

12. Y. You and W. Nam , *Chem. Sci.*, 2014, **5** , 4123 —4135.

13. S. Mandal , D. K. Poria , R. Ghosh , P. S. Ray and P. Gupta , *Dalton Trans.*, 2014, **43** , 17463 —17474.

14. C. Liu , L. Zhou , F. Wei , L. Li , S. Zhao , P. Gong , L. Cai and K. M. C. Wong , *ACS Appl. Mater. Interfaces*, 2019, **11** , 8797 —8806.

15. A. Sinopoli , F. A. Black , C. J. Wood , E. A. Gibson and P. I. P. Elliott , *Dalton Trans.*, 2017, **46** , 1520 —1530.

16. J. E. Laaser , J. R. Christianson , T. A. Oudenhoven , Y. Joo , P. Gopalan , J. R. Schmidt and M. T. Zanni , *J. Phys. Chem. C*, 2014, **118** , 5854 —5861.

17. T. Banerjee , S. Kaniyankandy , A. Das and H. N. Ghosh , *J. Phys. Chem. C*, 2013, **117** , 3084 —3092.

18. P. Paoprasert , S. Kandala , D. P. Sweat , R. Ruther and P. Gopalan , *J. Mater. Chem.*, 2012, **22** , 1046 —1053.

19. F. He , Y. Zhou , S. Liu , L. Tian , H. Xu , H. Zhang , B. Yang , Q. Dong , W. Tian , Y. Ma and J. Shen , *Chem. Commun.*, 2008, 3912 —3914.

20. P. K. Ng , X. Gong , S. H. Chan , L. S. M. Lam and W. K. Chan , *Chem. – Eur. J.*, 2001, **7** , 4358 —4367.

21. T. Yu , D. P. K. Tsang , V. K. M. Au , W. H. Lam , M. Y. Chan and V. W. W. Yam , *Chem. – Eur. J.*, 2013, **19** , 13418 —13427.

22. W. K. Chung , K. M. C. Wong , W. H. Lam , X. Zhu , N. Zhu , H. S. Kwok and V. W. W. Yam , *New J. Chem.*, 2013, **37** , 1753 —1767.

23. I. Chakraborty , S. J. Carrington and P. K. Mascharak , *ChemMedChem*, 2014, **9** , 1266 —1274.

24. P. Gómez-Iglesias , J. M. Martín-Alvarez , D. Miguel and F. Villafañe , *Dalton Trans.*, 2015, **44** , 17478 —17481.

25. V. Fernández-Moreira , I. Marzo and M. C. Gimeno , *Chem. Sci.*, 2014, **5** , 4434 —4446.

26. J. Yang , Q. Cao , H. Zhang , L. Hao , D. Zhou , Z. Gan , Z. Li , Y.-X. Tong , L.-N. Ji and Z.-W. Mao , *Biomaterials*, 2018, **176** , 94 —105.

27. A. Luengo , V. Fernández-Moreira , I. Marzo and M. C. Gimeno , *Inorg. Chem.*, 2017, **56** , 15159 —15170.

28. J. Yang , J. X. Zhao , Q. Cao , L. Hao , D. Zhou , Z. Gan , L. N. Ji and Z. W. Mao , *ACS Appl. Mater. Interfaces*, 2017, **9** , 13900 —13912.

29. A. Yazdani , N. Janzen , L. Banevicius , S. Czorny and J. F. Valliant , *Inorg. Chem.*, 2015, **54** , 1728 —1736.

30. M. W. Louie , H. W. Liu , M. H. C. Lam , Y. W. Lam and K. K. W. Lo , *Chem. – Eur. J.*, 2011, **17** , 8304 —8308.

31. F. L. Thorp-Greenwood , V. Fernández-Moreira , C. O. Millet , C. F. Williams , J. Cable , J. B. Court , A. J. Hayes , D. Lloyd and M. P. Coogan , *Chem. Commun.*, 2011, **47** , 3096 —3098.

32. J. R. Lakowicz , F. N. tellano , I. Gryczynski , Z. Gryczynski and J. D. Dattelbaum , *J. Photochem. Photobiol., A*, 1999, **122** , 95 —101.

33. Q. Ge , T. C. Corkery , M. G. Humphrey , M. Samoc and T. S. A. Hor , *Dalton Trans.*, 2009, 6192 —6200.

34. B. J. Coe , S. P. Foxon , R. A. Pilkington , S. Sánchez , D. Whittaker , K. Clays , N. Van Steerteghem and B. S. Brunschwig , *Organometallics*, 2016, **35** , 3014 —3024.

35. J. Nishida , C. Yan and M. D. Fayer , *J. Chem. Phys.*, 2017, **146** , 094201.

36. B. J. Coe , S. P. Foxon , R. A. Pilkington , S. Sánchez , D. Whittaker , K. Clays , G. Depotter and B. S. Brunschwig , *Organometallics*, 2015, **34** , 1701 —1715.

37. X. Yi , J. Zhao , J. Sun , S. Guo and H. Zhang , *Dalton Trans.*, 2013, **42** , 2062 —2074.

38. X. Yi , J. Zhao , W. Wu , D. Huang , S. Ji and J. Sun , *Dalton Trans.*, 2012, **41** , 8931 —8940.

39. J. M. Favale , E. O. Danilov , J. E. Yarnell and F. N. tellano , *Inorg. Chem.*, 2019, **58** , 8750 —8762.

40. M. Busby , F. Hartl , P. Matousek , M. Towrie and A. Vlček , *Chem. – Eur. J.*, 2008, **14** , 6912 —6923.

41. M. Fumanal , E. Gindensperger and C. Daniel , *J. Chem. Theory Comput.*, 2017, **13** , 1293 —1306.

42. S. Sato , Y. Matubara , K. Koike , M. Falkenström , T. Katayama , Y. Ishibashi , H. Miyasaka , S. Taniguchi , H. Chosrowjan , N. Mataga , N. Fukazawa , S. Koshihara , K. Onda and O. Ishitani , *Chem. – Eur. J.*, 2012, **18** , 15722 —15734.

43. R. Kinghat , G. Schmitt , K. Ciamala , A. Khatyr , M. Knorr , S. Jacquot-Rousseau , Y. Rousselin and M. M. Kubicki , *C. R. Chim.*, 2016, **19** , 320 —332.

44. S. Jacquot-Rousseau , A. Khatyr , G. Schmitt , M. Knorr , M. M. Kubicki and O. Blacque , *Inorg. Chem. Commun.*, 2005, **8** , 610 —613.

45. I. Chakraborty , J. Tena and P. K. Mascharak , *Inorg. Chim. Acta*, 2017, **467** , 358 —363.

46. S. Ye , W. Kaim , M. Albrecht , F. Lissner and T. Schleid , *Inorg. Chim. Acta*, 2004, **357** , 3325 —3330.

47. A. Knödler , M. Wanner , W. Kaim and J. Fiedler , *Z. Anorg. Allg. Chem.*, 2002, **628** , 1132.

48. A. Jackson , J. Davis , R. J. Pither , A. Rodger and M. J. Hannon , *Inorg. Chem.*, 2001, **40** , 3964 —3973.

49. E. W. Abel , D. Ellis and K. G. Orrell , *J. Chem. Soc., Dalton Trans.*, 1992, 2243 —2249.

50. S. Jacquot-Rousseau , G. Schmitt , A. Khatyr , M. Knorr , M. M. Kubicki , E. Vigier and O. Blacque , *Eur. J. Org. Chem.*, 2006, 1555 —1562.

51. R. Kinghat , A. Khatyr , G. Schmitt , M. Knorr , M. M. Kubicki , E. Vigier and F. Villafañe , *Inorg. Chem. Commun.*, 2008, **11** , 1060 —1063.

52. I. E. Pomestchenko , D. E. Polyansky and F. N. tellano , *Inorg. Chem.*, 2005, **44** , 3412 —3421.

53. D. R. Striplin and G. A. Crosby , *Coord. Chem. Rev.*, 2001, **211** , 163 —175.

54. D. Wang , Q. L. Xu , S. Zhang , H. Y. Li , C. C. Wang , T. Y. Li , Y. M. Jing , W. Huang , Y. X. Zheng and G. Accorsi , *Dalton Trans.*, 2013, **42** , 2716 —2723.

55. G. Ferraudi , M. Feliz , E. Wolcan , I. Hsu , S. A. Moya and J. Guerrero , *J. Phys. Chem.*, 1995, **99** , 4929 —4934.

56. P. J. Giordano and M. S. Wrighton , *J. Am. Chem. Soc.*, 1979, **101** , 2888 —2897.

57. M. Wrighton and D. L. Morse , *J. Am. Chem. Soc.*, 1974, **96** , 998 —1003.

58. M. Saldías , N. Guzmán , F. Palominos , C. Sandoval-Altamirano , G. Günther , N. Pizarro and A. Vega , *ACS Omega*, 2019, **4** , 4679 —4690.

59. A. Świtlicka-Olszewska , T. Klemens , I. Nawrot , B. Machura and R. Kruszynski , *J. Lumin.*, 2016, **171** , 166 —175.

60. R. Kinghat , H. Boudiba , A. Khatyr , M. Knorr and M. M. Kubicki , *Acta Crystallogr., Sect. E: Struct. Rep. Online*, 2008, **64** , o370 —o370.

61. (*a*) R. F. W. Bader *Acc. Chem. Res.*, 1985, **18** , 9 —15 . (*b*) R. Bader *Chem. Rev.*, 1991, **91** , 893 —928.

62. Y.-C. Yang , S.-T. Lin and C.-C. Cao , *J. Chin. Chem. Soc.*, 2007, **54** , 587 —594.

63. A. Amoedo-Portela , R. Carballo , J. S. as , E. García-Martínez , A. Sánchez-González , J. Sordo and E. M. Vázquez-López , *Polyhedron*, 2003, **22** , 1077 —1083.

64. J. Connolly , G. W. Goodban , G. Reid and A. M. Z. Slawin , *Dalton Trans.*, 1998, 2225 —2231.

65. J. Connolly , M. K. Davies and G. Reid , *Dalton Trans.*, 1998, 3833 —3838.

66. E. W. Abel , S. K. Bhargava , M. M. Bhatti , K. Kite , M. A. Mazid , K. G. Orrell , V. Šik , B. L. Williams , M. B. Hursthouse and K. M. A. Malik , *Dalton Trans.*, 1982, 2065 —2072.

67. P. Gómez-Iglesias , F. Guyon , A. Khatyr , G. Ulrich , M. Knorr , J. M. Martín-Alvarez , D. Miguel and F. Villafañe , *Dalton Trans.*, 2015, **44** , 17516 —17528.

68. A. Dinache , A. Smarandache , A. Simon , V. Nastasa , T. Tozar , A. Pascu , M. Enescu , A. Khatyr , F. Sima , M. L. Pascu and A. Staicu , *Appl. Surf. Sci.*, 2017, **417** , 136 —142.

69. A. El Nahhas , A. Cannizzo , F. Van Mourik , A. M. Blanco-Rodríguez , S. Záliš , A. Vlček and M. Chergui , *J. Phys. Chem. A*, 2010, **114** , 6361 —6369.

70. A. Cannizzo , A. M. Blanco-Rodríguez , A. El Nahhas , J. Šebera , S. Záliš , A. Vlček and M. Chergui , *J. Am. Chem. Soc.*, 2008, **130** , 8967 —8974.

71. C. Gourlaouen , J. Eng , M. Otsuka , E. Gindensperger and C. Daniel , *J. Chem. Theory Comput.*, 2015, **11** , 99 —110.

72. Y. Harabuchi , J. Eng , E. Gindensperger , T. Taketsugu , S. Maeda and C. Daniel , *J. Chem. Theory Comput.*, 2016, **12** , 2335 —2345.

73. A. El Nahhas , C. Consani , A. M. Blanco-Rodríguez , K. M. Lanter , O. Braem , A. Cannizzo , M. Towrie , I. P. Clark , S. Záliš , M. Chergui and A. Vlček , *Inorg. Chem.*, 2011, **50** , 2932 —2943.

74. L. C. Abbott , C. J. Arnold , T. Q. Ye , K. C. Gordon , R. N. Perutz , R. E. Hester and J. N. Moore , *J. Phys. Chem. A*, 1998, **102** , 1252 —1260.

75. A. Gabrielsson , M. Busby , P. Matousek , M. Towrie , E. Hevia , L. Cuesta , J. Perez , S. Záliš and A. Vlček , *Inorg. Chem.*, 2006, **45** , 9789 —9797.

76. M. S. Jana , A. K. Pramanik , S. Kundu , D. Sarkar and T. K. Mondal , *Inorg. Chim. Acta*, 2013, **399** , 138 —145.

77. P. Christensen , A. Hamnett , A. V. G. Muir and J. A. Timney , *J. Chem. Soc., Dalton Trans.*, 1992, 1455 —1463.

78. T. T. Zhang , J. Jia and H. S. Wu , *Theor. Chem. Acc.*, 2012, **131** , 1 —8.

79. D. Chen De Ramkrishna and D. L. Mohler , *Synthesis*, 2009, 211 —216.

80. Y. Chen , W. Liu , J. S. Jin , B. Liu , Z. G. Zou , J. L. Zuo and X. Z. You , *J. Organomet. Chem.*, 2009, **694** , 763 —770.

81. P. D. Harvey and M. Knorr , *Macromol. Rapid Commun.*, 2010, **31** , 808 —826.

82. P. D. Harvey and M. Knorr , *J. Cluster Sci.*, 2015, **26** , 411 —459.

83. P. D. Harvey and M. Knorr , *J. Inorg. Organomet. Polym. Mater.*, 2016, **26** , 1174 —1197.

84. F. Juvenal , A. Langlois , A. Bonnot , D. Fortin and P. D. Harvey , *Inorg. Chem.*, 2016, **55** , 11096 —11109.

85. F. Juvenal , A. Bonnot , D. Fortin and P. D. Harvey , *ACS Omega*, 2017, **2** , 7433 —7443.

86. F. Juvenal and P. D. Harvey , *J. Inorg. Organomet. Polym. Mater.*, 2020, **30** , 159 —168.

87. A. Raghuvanshi , C. Strohmann , J. B. Tissot , S. Clément , A. Mehdi , S. Richeter , L. Viau and M. Knorr , *Chem. – Eur. J.*, 2017, **23** , 16479 —16483.

88. H. N. Peindy , F. Guyon , A. Khatyr , M. Knorr , V. H. Gessner and C. Strohmann , *Z. Anorg. Allg. Chem.*, 2009, **635** , 2099 —2105.

89. H. N. Peindy , F. Guyon , I. Jourdain , M. Knorr , D. Schildbach and C. Strohmann , *Organometallics*, 2006, **25** , 1472 —1479.

90. W. D. Dolling , K. F. Frost , F. H. Heinemann and H. H. Hartung , *Z. Naturforsch., B: J. Chem. Sci.*, 1993, **48** , 493 —504.

91. D. Vitali and F. Calderazzo , *Gazz. Chim. Ital.*, 1972, **102** , 587 —596.

92. K. Moedritzer *Synth. React. Inorg. Met.-Org. Chem.*, 1971, **1** , 63 —68.

93. S. Jacquot , A. Belaissaoui , G. Schmitt , B. Laude , M. M. Kubicki and O. Blacque , *Eur. J. Org. Chem.*, 1999, 1541 —1544.

94. M. J.Frisch, *et al.*, Gaussian 09 Revision B.01, Gaussian Inc., Wallingford, CT, 2013.

95. P. Hohenberg and W. Kohn , *Phys. Rev.*, 1964, **136** , B864.

96. W. Kohn and L. J. Sham , *Phys. Rev.*, 1965, **140** , A1133.

97. R. G. Parr and W. Yang , *Density-functional theory of atoms and molecules* , Oxford University Press, 1989.

98. *The Challenge of d and f Electrons* , D. R. Salahub and M. C. Zerner, American Chemical Society, Washington, DC, 1989, vol. 394.

99. R. Bauernschmitt and R. Ahlrichs , *Chem. Phys. Lett.*, 1996, **256** , 454 —464 .

100. M. E. ida , C. Jamorski , K. C. ida and D. R. Salahub , *J. Chem. Phys.*, 1998, **108** , 4439 —4449.

101. R. E. Stratmann , G. E. Scuseria and M. J. Frisch , *J. Chem. Phys.*, 1998, **109** , 8218 — 8224.

102. C. Lee , W. Yang and R. G. Parr , *Phys. Rev. B: Condens. Matter Mater. Phys.*, 1988, **37** , 785 —789.

103. B. Miehlich , A. Savin , H. Stoll and H. Preuss , *Chem. Phys. Lett.*, 1989, **157** , 200 — 206.

104. B. P. Pritchard , D. Altarawy , B. Didier , T. D. Gibson and T. L. Windus , *J. Chem. Inf. Model.*, 2019, **59** , 4814 —4820.

105. D. Feller *J. Comput. Chem.*, 1996, **17** , 1571 —1586.

106. K. L. Schuchardt , B. T. Didier , T. Elsethagen , L. Sun , V. Gurumoorthi , J. Chase , J. Li and T. L. Windus , *J. Chem. Inf. Model.*, 2007, **47** , 1045 —1052.

107. N. M. O'Boyle , A. L. Tenderholt and K. M. Langner , *J. Comput. Chem.*, 2008, **29** , 839 —845.

108. Z. Otwinowski and W. Minor , *Methods Enzymol.*, 1997, **276** , 307 —326.

109. A. Altomare , G. carano , C. Giacovazzo and A. Guagliardi , *J. Appl. Crystallogr.*, 1993, **26** , 343 —350.

110. L. Palatinus and G. Chapuis , *J. Appl. Crystallogr.*, 2007, **40** , 786 —790.

111. G. M. Sheldrick *Acta Crystallogr., Sect. C: Struct. Chem.*, 2015, **71** , 3 —8.

112. R. H. Blessing *Acta Crystallogr., Sect. A: Found. Crystallogr.*, 1995, **51** , 33 —38.

113. Brucker, APEX3, SADABS and SAINT, Bruker AXS Inc., Madison, Wisconsin, USA, 2016.

114. O. V. Dolomanov , L. J. Bourhis , R. J. Gildea , J. A. K. Howard and H. Puschmann , *J. Appl. Crystallogr.*, 2009, **42** , 339 —341.

Footnotes

Dedicated to the memory of our colleague Prof. Mironel Enescu, deceased in 2020.

Electronic supplementary information (ESI) available: Representation of secondary interactions, atomic contributions of the various fragments to the frontier MOs, electron-density differences, representations of the frontier MOs, calculated positions, oscillator strengths and major contributions of the first 100 singlet–singlet electronic transitions, emission decay in 2-MeTHF at 77 K, photophysical properties, simulated absorption spectrum by TDDFT computations of **L6**, **1a–c**, **1e–j** and cyclic voltammograms recorded for **1b** and **1h**.